Glacier Energy and Mass Balance (GEMB): A model of firn processes for cryosphere research

Alex S. Gardner[1], Nicole-Jeanne Schlegel[1], Eric Larour[1]

[1]Jet Propulsion Laboratory, California Institute of Technology, Pasadena, 91109, United States of
America

Correspondence to: Alex S. Gardner (alex.s.gardner@jpl.nasa.gov)

Abstract. This paper provides the first description of the open-source Glacier Energy and Mass Balance
model. GEMB models the ice sheet and glacier surface-atmospheric energy and mass exchange, and
firn state. It is a column model (no horizontal communication) of intermediate complexity that includes
those processes deemed most relevant to glacier studies with the goal of retaining computational
efficiency that can accommodate the very long (thousands of years) spin-ups necessary for initializing
deep firn columns and for running sensitivity experiments to characterize model uncertainty on
continental scales. The model is one-way coupled with the atmosphere which allows the model to be
run off-line with a diversity of climate forcing but neglects feedback to the atmosphere. GEMB
provides numerous parameterization choices for various key processes (e.g. albedo, subsurface
shortwave absorption, and compaction), making it well suited for uncertainty quantification and model
exploration. The model is evaluated against the current state-of-the-art and in situ observations and is
shown to perform well.

1. Introduction

The near surface (upper most tens to hundreds of meters depth) energy and mass budget of mountain
glaciers, icefields, ice caps and ice sheets (i.e. glaciers) is controlled by complex interactions between
clouds, the atmospheric boundary layer, the ice surface, and processes internal to the ice-air matrix (cf.
Munro & Davies, 1977; Colbeck, 1982; Wiscombe & Warren, 1980; van den Broeke et al, 1994;
Greuell & Konzelmann, 1994). It all starts with the nucleation of supercooled water vapor around
impurities in the atmosphere that form highly dendritic ice crystals that become heavy and fall from the
atmosphere and deposit on the glacier surface forming a highly reflective, insulative, and low-density
surface layer. Over time, ice crystals tend towards a shape that minimizes surface area through vapor
diffusion and mechanical breakage, rounding the crystals, reducing reflectance (cf. Brun, 1989; Flanner
& Zender, 2016; Gardner et al. 2010) and increasing both density and thermal conductivity (e.g.
Calonne et al., 2019). The rate at which the metamorphism takes place depends on both the mean
temperature and vertical gradients in temperature (e.g. Herron and Langway, 1980; Arthern et al.,
2010). This layer will become buried by successive snowfalls, subjecting it to increasing overburden
stress that causes the crystals to slide and compact, further increasing both density and conductivity as
the snow transitions to firn. Sliding of crystals tends to control the rate of compaction as the firn

35   approaches a density of ~550 km m^{-3} after which the migration of grain boundaries, through sintering processes, controls the rate of compaction to the point at which the air within the ice matrix becomes sealed off from the surrounding pore space at a density of ~830 kg m^{-3} (cf. Herron and Langway, 1980; Alley, 1987). Beyond a density of 830 kg m^{-3}, compaction is regulated by the compression of the air within the sealed pore space.

40

    Under most conditions, net solar radiation is the largest input of energy for melting of ice (cf. Male and Granger, 1981). The amount of solar energy absorbed is largely governed by the effective grain size of the snow crystals within the top few centimeters of the surface, in combination with the concentration and placement of light absorbing impurities (cf. Gardner & Sharp, 2010; Warren & Wiscombe, 1980).

45   This dependency can create strong positive feedbacks in the energy balance wherein increased solar input leads to enhanced grain growth that in turn results in increased shortwave absorption, modified thermal gradients, enhanced compaction and increased thermal conductivity. The introduction of melting decreases the number of ice-air boundaries which reduces scattering and further enhances absorption of shortwave radiation (cf. Gardner & Sharp, 2010). If melting is sufficient to overcome

50   capillary forces it will descend vertically within the snow/firn column redistributing large amounts of energy though latent heat release upon freezing or mass though encountering an impermeable surface and moving horizontally within the firn (cf. Coléou & Lesaffre, 1998; Marchenko et al., 2017). This complex interplay of surface processes creates non-linear responses to changes in surface forcing that require detailed modeling of the underlying physical processes.

55

    Modern firn modeling draws heavily on the model physics implemented within seasonal snow models that have been developed for hydrology applications and avalanche forecasting. A few of the more widely used snow models include SNOWPACK (Bartelt & Lehning, 2002), CROCUS (Brun et al., 1989) and SnowModel (Liston and Elder, 2006). For a more comprehensive discussion of processes

60   relevant for modeling of seasonal snow, readers should refer to the provided references and those that follow. Here we review those aspects relevant to modeling of perennial firn over ice sheets.

    Early numerical modeling of firn was motivated by ice core research with an emphasis on understanding bore-hole temperature and pore close-off that is needed to determine the ice-age gas-age

65   differential (e.g. Herron and Langway, 1980; Greuell & Oerlemans, 1989). Since, firn models have become critical to the estimation of the surface mass budget of the ice sheets (e.g. Pfeffer et al. 1991; Janssens & Huybrechts, 2000) as they are needed to model the vertical movement of meltwater within the snow and firn, and to determine if the meltwater refreezes in place or moves horizontally following the hydrologic gradient (Marsh & Woo, 1984; Pfeffer et al. 1990). Subsequent firn modeling efforts

70   suggest that a warming climate will result in a steady decrease in the Greenland Ice Sheet's capacity to retain meltwater due to a reduction in firn pore space (van Angelen et al., 2013), a finding that has been supported by in situ observations (Vandecrux et al., 2019). Further, impermeable ice layers formed at depth within the firn can support perched aquifers or enhance metlwater runoff (Culberg et al., 2021; Miller et al., 2022; Macferrin et al., 2019). Recent observations of extensive "firn aquifers" in

75   Greenland that persist throughout the winter, when snow accumulation and melt rates are high (Forster

et al., 2014), have proven the utility of firn modeling for understanding newly discovered phenomena (Steger et al., 2017).

With the launch of the first satellite altimeters in the late-1970s it became possible, for the first time, to measure large-scale changes in ice sheet topography (Zwally et al., 1989). However, the interpretation of such changes was challenging due to unknown changes near-surface snow and firn density (Van Der Veen, 1993). The challenge is that changes in the near-surface density (i.e. changes in the firn air content: FAC) can cause changes in surface elevation without any corresponding changes in mass. By the late 1990s, numerical firn models were being used to estimate the uncertainties in the conversion of elevation change to mass change (Arthern & Wingham, 1998) and by the mid-2000s were being used to estimate the ice sheet wide changes in FAC for ice sheet wide estimation of mass change from satellite altimetry data (Zwally et al., 2005). Despite significant advances in firn modeling over the past decade and a half (e.g. Bougamont & Bamber, 2005; Ligtenberg et al., 2011), models still have significant deficits (Lundin et al., 2017; Vandecrux et al., 2020) and remain the largest source of uncertainty when inferring ice sheet mass change from satellite altimetry (Smith et al., 2019).

Here we present a new coupled surface energy balance and firn model, the Glacier Energy and Mass Balance model (GEMB, the "B" is silent) that has been integrated as a module into the Ice-sheet and Sea-level System Model (ISSM). Here we describe the state of GEMB as of Version 1.0. ISSM is an open-source software framework for modeling ice sheets, solid earth, and sea-level response that is developed at NASA's Jet Propulsion Laboratory (JPL) in conjunction with the University of California, Irvine and Dartmouth College (Larour et al., 2012). The Dakota software (https://dakota.sandia.gov) is embedded within the ISSM framework, facilitating uncertainty quantification and sensitivity studies (Larour et al., 2012a,b; Schlegel et al., 2013,2015; Schlegel and Larour, 2019). Currently GEMB is a stand-along module that is responsible for the calculation of ice sheet and glacier surface-atmospheric energy and mass exchange and firn state within ISSM. GEMB provides the ice sheet flow model with near-surface ice temperature and mass flux boundary conditions. It is a column model (no horizontal communication) of intermediate complexity that includes those processes deemed most relevant to glacier studies with the goal of retaining computational efficiency that can accommodate the very long (thousands of years) spin-ups necessary for initializing deep firn columns and for running sensitivity experiments to characterize model uncertainty on continental scales. GEMB is not coupled with a model of the atmosphere and instead runs offline, forced with climate reanalysis or climate model data. This approach allows flexibility in selection of forcing datasets at the expense of simulating surface-atmosphere feedbacks.

GEMB is currently run independently of the ice flow model. The goal is to eventually couple the ice flow model with GEMB. In this situation the flow model would provide the 3-D surface displacement vectors to GEMB to inform the advection of the column nodes relative to the climate forcing and to allow for solving of longitudinal stretching of the firn. Currently the major hurdle for coupling the models is the implementation of downscaling routines for the climate forcing.

2. Model Description

GEMB is a vertical 1-D column model, i.e. no horizontal communication between model nodes, that simulates atmosphere-surface mass and energy exchanges and the internal evolution of snow, firn and ice. The model shares many characteristics with earlier published firn models that also simulate atmosphere-surface exchanges (e.g. Bassford, 2002; Bougamont & Bamber, 2005; Greuell & Konzelmann, 1994). The model is a finite-difference model with tens to hundreds of layers, the thickness of which are managed dynamically. It is forced at its surface with near-surface (2-10 m) estimates of precipitation, air temperature, wind speed, vapor pressure, surface pressure, and downwelling longwave and shortwave radiation fluxes and optional inputs of solar zenith angle, cloud optical thickness and bare ice albedo. At its bottom boundary, the model applies a constant thermal flux. Internally, the model simulates thermal diffusion, shortwave sub-surface penetration, meltwater retention, percolation and refreeze, effective snow grain size, dendricity, and sphericity, and compaction. The model does not yet account for changes in firn due to horizontal advection of divergence of the ice (Horlings et al., 2021). GEMB also does not account for changes in thermal properties caused by debris cover that are important for the modeling of valley glaciers. In this section we detail specific implementation of various processes, and their options, within the model.

2.1. Layer Initialization

GEMB is a finite difference model that simulates the snow-firn-ice as a number of discrete plane-parallel vertical layers, each with their own state parameters. The thickness (dz) of each vertical layer is initialized according to default or user supplied specification of the minimum and maximum thickness. Firn properties and energy fluxes have more vertical heterogeneity nearer the surface-atmosphere boundary than deeper within the firn column. Because of this the near-surface firn must be modeled using finer model layers than those deeper within the firn column, where energy fluxes small and gradients in ice properties are more diffuse. To accommodate this, finer model layers are specified for the near-surface. Layers below the near-surface are assigned increasing layer thickness with depth. Layer thickness is increased with depth to minimize the overall number of layers needed to simulate the firn column, improving computational efficiency without sacrificing accuracy. User can specify the maximum near-surface thickness (dz_{top}, default = 0.05 m), the depth of the near-surface (z_{top}, default = 10 m), the maximum column depth (z_{max}, default = 250 m) and a unitless scaling by depth parameter (β, default = 1.025). The thickness of each layer and the depth of the snow-firn-ice column is then determined as shown in Figure 1. The user can also specify a minimum near-surface thickness (dz_{min}) and a minimum column depth (z_{min}). If a layer thins to less than dz_{min} then it is combined with the layer directly below. If the total depth of the column is less than z_{min} then an additional ice layer is added to the bottom of the column.

2.2. Grain Growth

The model's master time step (i.e. the time step for all processes excluding the thermal model) is set by the timestep of the input data (typically on the order of hours). For all time steps, the first calculation of the GEMB model is done by the grain growth module. This module tracks and evolves the effective

grain radius, dendricity, and sphericity of all model layers through time. These properties evolve
155 according to published laboratory estimates for dendritic (Brun et al., 1992, Equations 3 & 4), non-dendritic (Marbouty, 1980, Figure 9), and wet snow metamorphism (Brun, 1989, Figure 6) that are dependent on mean layer temperature and density, and on gradients in temperature.

2.3. Shortwave flux

After the grain properties of all model layers are determined, GEMB runs the albedo module. GEMB
160 provides five methods for calculating broadband surface albedo. The default albedo scheme is after Gardner and Sharp (2009), where albedo is calculated as a function of grain specific surface area ($\hat{S}$), concentration of light-absorbing carbon (c: optional), solar zenith angle (u': optional), and cloud optical thickness (τ: optional):

$$\alpha = \alpha_{\hat{s}} + d\alpha_c + d\alpha_{u'} + d\alpha_\tau \qquad (1)$$

165
Where $\alpha_{\hat{s}}$ is the pure snow albedo, $d\alpha_c$ is the change in albedo due to the presence of light-absorbing carbon, $d\alpha_{u'}$ is the change in albedo due changes in the solar zenith angle, and $d\alpha_\tau$ is the change in albedo due to changes in the cloud optical thickness. Equations for each of the 4 components that sum to the net broadband albedo are provided in Equations 7 - 11 in Gardner and Sharp (2009).

170
Surface broadband albedo can also be calculated based on the effective grain radius (r_e), where broadband albedo is determined as a summation of the albedo within three spectral bands of solar irradiance (Brun et al., 1992, Lefebre et al., 2003). Effective grain radius can be related to specific surface area as:

175

$$r_e = \frac{3}{\rho_i \hat{S}} \qquad (2)$$

Where ρ_i is the density of ice (910 kg m^{-3}).

Additionally, the surface albedo can be parameterized as a function of snow density and cloud amount
180 according to Greuell & Konzelmann (1994) or as combination of exponential time decay and firn wetness following Bougamont & Bamber (2005). A detailed review of all mentioned albedo schemes can be found in Section 4.2 of Gardner et al., 2009.

The albedo of bare ice (defined by a density threshold, default of 820 kg m^{-3}) can be set as a constant
185 everywhere or spatially varying when specified for each model node (e.g. as derived from MODIS). Alternatively, the ice albedo and shallow snow-covered (<10 cm in depth) ice albedo can be parameterized as a function of model-estimated accumulation of surface meltwater following Equation 5 of Alexander et al. (2014).

5

190   When shortwave radiation reaches the glacier surface it is scattered and absorbed. The fraction of
       energy that is scattered then reflected back to the atmosphere is dictated by the modeled broadband
       albedo. The remainder of the energy is absorbed within the snow, firn and ice. By default, GEMB will
       allocate all absorbed energy to the top model layer (subsurface absorption turned off) but also allows for
       the absorbed radiation to be distributed within near-surface (i.e. across multiple near surface layers:
195   subsurface absorption turned on). When the subsurface absorption is turned on, the amount of
       shortwave radiation absorbed within each model layer is dependent on which albedo scheme is used. If
       the albedo scheme is based on effective grain radius, then the subsurface absorption is calculated in
       three spectral bands, dependent on effective grain radius as described by Brun et al. (1989, pages 333-
       334). In all other cases, the subsurface albedo is treated as a function of each layer's snow density
200   (Bassford, 2002, Equation 4.15). In this case a specified fraction of the shortwave radiation
       (approximately 36%) is absorbed by the surface layer (Greuell and Konzelmann, 1994), with the rest of
       the energy being absorbed at depth with consideration to Beer's law (Bassford, 2002).

2.4. Thermodynamics

       The thermodynamics module is responsible for determining the temperature of the snow, firn, and ice.
205   Temperature evolves according to thermal diffusion, in response to radiative, sensible and latent heat
       fluxes. The thermal conductivity of snow and ice is calculated according to Sturm et al. 1997 (default)
       or Calonne et al., 2011. GEMB calculates thermal diffusion using an explicit forward in time, central in
       space method (Patankar 1980, Ch. 3&4):

$$T_p = \frac{A_u * T_{u\circ} + A_d * T_{d\circ} + (A_p - A_u - A_d) * T_{p\circ} + S}{A_p} \tag{3}$$

210   where neighbor coefficients A_u, A_p, & A_d are

$$A_u = \left(\frac{dz_u}{2K_p} + \frac{dz_p}{2K_u}\right)^{-1}$$

$$A_d = \left(\frac{dz_d}{2K_p} + \frac{dz_p}{2K_d}\right)^{-1}$$

$$A_p = \frac{\rho * CI * dz}{dt}$$

       And subscripts u and d represent grid points up and down from the center grid point p and $\circ$ identifies
       previous time step values. S is a source term. dz is layer widths, ρ is layer density, dt is the time step, K
       is effective thermal conductivity, and CI is the heat capacity of ice.

215   The thermal diffusion calculation is executed at a much finer timestep (dt) than the master timestep, 10s
       of seconds versus hours. The finer time step is required to satisfy the Courant–Friedrichs–Lewy
       condition, a necessary condition to ensure numeric stability of the thermal solution when using an
       explicit forward in time method (Courant et al., 1928). See Patankar (1980) for an overview of
       numerical heat transfer and stability criterion for explicit forward methods. The small timestep for the
220   thermal diffusion makes this module, by far, the most computationally expensive component of GEMB.

The thermal module is looped within each GEMB timestep and therefore the thermal time step must divide evenly into the model's master time step. The effective thermal conductivity (k_{eff}) is calculated as a function of density according to Sturm et al. (1997, Equation 4), for densities < 910 kg m^{-3}:

$$k_{eff} = 0.138 - 1.01 * 10^{-3} * \rho + 3.233 * 10^{-6} * \rho^2 \qquad (4)$$

225 where ρ is the layer density in units of kg m^{-3}.

The effective thermal conductivity can also be calculated according to Calonne et al. (2011):

$$k_{eff} = 0.024 - 1.23 * 10^{-4} * \rho + 2.5 * 10^{-6} * \rho^2 \qquad (5)$$

230

For densities >= 910 kg m^{-3} effective thermal conductivity is calculated as a function of temperature:

$$k_{eff} = 9.828 * e^{-5.7*10^{-3}*T} \qquad (6)$$

where T is the layer temperature in Kelvin.

235 The minimum acceptable thermal timestep is calculated, dependent upon the thermal conductivity, and then divided by a scaling-factor to achieve numerical stability. Within every timestep, the thermal module calculates the diffusion of temperature within the snow, firn and ice.

At each thermal diffusion timestep the module determines the radiative and turbulent fluxes (Patterson,
240 1994; Murphy and Koop, 2005), rates of evaporation/condensation, and the new temperature profile throughout the model depth. Layer temperatures are allowed to artificially exceed the melting point of ice (273.15 K), the thermal energy above which is later converted to melt by the melt module. That said, the surface temperature used for computing the outgoing longwave energy and turbulent heat flux is taken as the lesser of the temperature of the top model layer or 273.15 K. The snow/ice is assumed to be
245 a grey body (default emissivity = 0.97) with the incoming longwave radiation absorbed within the top layer and outgoing longwave radiation calculated using the Stefan-Boltzmann constant (5.67E-8 W m^{-2} K^{-4}). Calculation of turbulent fluxes is defined in the next subsection. At the end of the thermodynamics module, any mass lost/added by evaporation/condensation is removed/added to the top layer.

250 **2.5. Turbulent Flux**

Turbulent fluxes and evaporation/sublimation/condensation are computed within the thermodynamics module using the bulk method. Turbulent fluxes are dependent on the atmospheric stratification (i.e. stability), which can be quantified through, for example, the bulk Richardson number, *Ri*:

$$Ri = \frac{2 * g * (z_v - z_0) * (T_a - T_s) * \left(\frac{1e5}{p_{air}}\right)^{0.286}}{z_T * (T_a + T_s) * \left(\frac{v}{z_v}\right)^2} \tag{7}$$

where g is the acceleration due to gravity (9.81 m s^{-2}), z_v is the height in meters at which the windspeed
255 (v) was measures, z_0 is the surface roughness in meters, T_a is the air temperature at z_v and T_s is the
surface temperature, both in Kelvin. p_{air} is the air pressure in Pascals. This is the bulk version of
Högström (1996: Eq. 9).

The bulk transfer coefficient is calculated based on momentum roughness length and the height at
260 which air temperature and wind speed inputs are provided. The momentum roughness length is set to
0.12 mm for dry snow, 1.3 mm for wet snow and 3.2 mm for ice, after Bougamont et al. (2005), and the
humidity and temperature roughness lengths are set to 10% of these values (Foken, 2008). Within each
thermodynamics time step, the model calculates the bulk Richardson number (Ri) and determines the
Monin-Obukhov stability parameters for weighting the sensible and latent heat flux. In stable conditions
265 (i.e., Ri>0), the stability weighting parameters are determined after Beljaars and Holtslag (1991) (Ding
et al., 2020, Equations 12 and 13), and in unstable conditions (i.e., $Ri <= 0$), the stability weighting
parameters are determined after Högström (1996) as in Sjöblom (2014, Equations 26 and 27). To
determine the latent heat flux, the model calculates the surface vapor pressure for liquid water or ice
(Murphy and Koop, 2005), depending on whether the surface is wet (Murray, 1967) or dry (Bolton,
270 1980), respectively. The sensible and latent heat are then determined as a function of the bulk transfer
coefficient and the Monin-Obukhov stability parameters, and model inputs of surface temperature
(lesser of the temperature of the top model layer or 273.15 K), near-surface air temperature, near-
surface wind speed, near-surface vapor pressure, and the air pressure at the surface. Mass transfer due to
evaporation/sublimation/condensation is based on the latent heat flux along with the latent heat of
275 evaporation/condensation (gas <-> liquid) or the latent heat of sublimation (solid <-> gas).

2.6. Accumulation

The GEMB accumulation module is responsible for the addition of mass due to precipitation and related
modification of uppermost layer properties (i.e. density, temperature, dendricity, sphericity, and grain
280 radius). When precipitation occurs and the air temperature is below the melting point, the model
accumulates precipitation as snow at the surface. The density of newly fallen (ρ_0) snow can be set to a
default value, i.e., 350 kg/m^3 (Weinhart et al., 2020) for Antarctica or 315 kg/m^3 (Fausto et al., 2018)
for Greenland, or it can be parameterized as a function of the annual temperature, accumulation, surface
pressure and wind speed according to Kaspers et al. (2004):
285

$$\rho_0 = 7.36 * 10^{-2} + 1.06 * 10^{-3} * T_s + 6.69 * 10^{-2} * A + 4.77 * 10^{-3} * v \tag{8}$$

where T_s is the annual surface temperature in Kelvin, A is the average annual accumulation in m w.e.,
and v is the annual mean windspeed in m s^{-1} measured 10 m above the surface.

290   ρ_0 can also be modeled as a function of annual air temperature according to Kuipers Munneke et al. (2015):

$$\rho_0 = 481 + 4.834 * (T_s - 273.15) \tag{9}$$

By default, fresh snow dendricity is set to 1 and fresh snow sphericity is set to 0.5. For Greenland, we
295   consider wind effects on the snow's initial dendricity and sphericity following Guyomarc'h and Merindol (1998) as in Vionnet et al. (2012). In the case where the air temperature is at or exceeds the melting point, precipitation is treated as rain, and liquid water is added to the uppermost model layer. When this occurs, the surface layer properties, specifically temperature and density, are updated to account for the addition of mass as ice and the release of latent heat. Any thermal energy exceeding the
300   melting point of ice will be converted back to liquid water by the melt module and allowed to percolate. The approach of adding rain as ice plus latent heat of refreeze, and later converting back to liquid water if the top firn layer does not possess enough cold content to freeze the rain in place, is simply for computational convenience.

305   If the newly accumulated mass exceeds the minimum allowable top-layer layer thickness (dz_{min}), the accumulation is added as a new surface layer. Otherwise, the snow is added to the existing surface layer, and the surface properties are adjusted to accommodate the accumulation by averaging properties, weighting by mass, with the exception of dendricity and sphericity, which take the value of the newly accumulated snow. New snow that is accumulated is assumed to have the same temperature as the near-
310   surface air temperature. GEMB does not account for mass transport due to wind.

2.7. Melt

After new mass is accumulated within the top layer(s), the melt module is run. This module is responsible for calculating how much melt will occur throughout the model column, how much of the melt will percolate into layers below, how much of this melt will refreeze, how much of the melt will
315   runoff, and how the temperature of each layer will evolve accordingly. GEMB uses a bucket scheme (cf. Steger et al., 2017) to model the vertical movement of meltwater within the firn. The first step of this scheme is to determine how much of the current pore water in the firn column can be refrozen without heating the firn layer above the freezing point of ice. If this water does exist, it is refrozen locally, and the model layers' physical and thermal properties are updated in response to this process.
320   The next step is to determine where melt will occur. Beginning with the surface layer, the module determines if the local thermal energy is capable of melting any of the ice within the layer, and if it is, this portion of the layer is melted and any excess thermal energy (i.e. all ice in layer is melted) or melt water exceeding the irreducible water content (i.e. water held in place by capillary effects) is redistributed to the layer below. The irreducible water content is assumed to be 7% of the pore volume
325   according to Colbeck, 1972. As the meltwater is distributed to lower layers, it may reach a layer of impermeability (density of pore hole close-off, ~830 kg/m³), and at this point, that meltwater exits the system and is considered runoff. If the layer into which the meltwater flows is permeable and the

capillary effects can retain the incoming meltwater, the water is held within that layer and is combined with any pre-existing liquid water. If any portion of the incoming meltwater cannot be accommodated
330 within the layer, it percolates (instantaneously) to the layer below. Water that remains is refrozen locally, within each layer, but only until the local temperature reaches the freezing point (273.15 K). Meltwater that reaches the deepest layer of the column exits the system and is considered by the model to be runoff. Runoff values from all layers of a column are summed to determine the total amount of melt that runs off (i.e. exits the model domain). GEMB does not model currently model firn aquifers as
335 any water exceeding the irreducible water content is removed from the system once it encounters an impermeable ice layer. Modifying GEMB to simulate firn aquifers would simply require the addition of a slope dependent runoff criterion.

2.8. Layer Management

After the melt/refreeze/runoff calculations are complete, the melt module ensures that the thickness of
340 any single layer does not exceed thresholds set for the minimum and maximum allowable layer thickness. This is done through the merging or splitting of model layers and associated changes in layer properties. Specifically, this module ensures that layering within the column adheres to: the user-defined minimum thickness for a layer (dz_{min}); the user-defined maximum change in depth between adjacent layers (β, default = 1.025 or 2.5% change between layers); and the user-defined maximum
345 (z_{max}) and minimum (z_{min}) depths of the total column (with default values of 250 m and 130 m, respectively). Before completion, the melt module checks for the conservation of mass and energy, and throws an error if these values are not conserved. If the maximum column depth is exceeded, mass is removed from the bottom layer. If the depth of the model falls below the minimum allowable depth, then ice is added to the bottom layer of the model with identical properties as possessed by the bottom
350 layer. All additions and subtractions of mass are cataloged and accounted for in final mass change estimates (i.e. not included in estimates of surface mass balance).

2.9. Compaction

After the merging/splitting of model layers, GEMB runs the densification module. This module calculates how much the snow and firn layers compact (increase in density) over the master time step.
355 Compaction ($d\rho$) is determined following Herron and Langway (1980):

$$d\rho = c * (\rho_{ice} - \rho°) * dt \tag{10}$$

Where $d\rho$ is the change in layer density in kg m^{-3}, c is the rate parameter, ρ_{ice} is the density of ice (910 kg m^{-3}), $\rho°$ is the layer density from the previous time step, and dt is the time interval. $c = c0$ for
360 density <= 550 kg/m^3 and $c = c1$ for densities between 550 kg/m^3 and 830 kg/m^3.

The densification module offers five different approaches for computing compaction rate factors:
1. Herron and Langway (1980):

$$c0 = 11 * e^{\frac{-10160}{T*R}} * \frac{C}{\delta_{water}}$$

$$c1 = 575 * e^{\frac{-21400}{T*R}} * \sqrt{\frac{C}{\delta_{water}}}$$

(11)

where T is the layer temperature in K, R is the gas constant (8.314 J K^{-1} mol^{-1}), C is the average annual accumulation in kg m^{-2} yr^{-1}, and δ_{water} is the density of water (1000 kg m^{-3}).

2. Arthern et al. (2010) (semi-empirical):

$$c0 = 0.07 * e^{\frac{-E_c}{T*R}+\frac{E_g}{T_{mean}*R}} * C * g$$

$$c1 = 0.03 * e^{\frac{-E_c}{T*R}+\frac{E_g}{T_{mean}*R}} * C * g$$

(12)

where E_c is the activation energy for self-diffusion of water molecules through the ice lattice (60 kJ mol^{-1}), E_g is the activation energy for grain growth (42.4 kJ mol^{-1}), T_{mean} is the mean annual temperature in K, and g is the acceleration due to gravity (9.81 m s^{-1}).

3. Arthern the al. (2010) (physical model):

$$c0 = 9.2 * 10^{-9} * e^{\frac{-Ec}{T*R}} * \frac{\sigma}{r_e^2}$$

$$c1 = 3.7 * 10^{-9} * e^{\frac{-Ec}{T*R}} * \frac{\sigma}{r_e^2}$$

(13)

where r_e is the effective grain radius in meters (see Equation 2).

4. Li and Zwally (2004):

$$c0 = c1 = \frac{C}{\rho_{ice}} * (139.21 - 0.542 * T_{mean}) * 8.36 * (273.15 - T)^{-2.061}$$

(14)

5. and Helsen et al. (2008):

$$c0 = c1 = \frac{C}{\rho_{ice}} * (76.138 - 0.28965 * T_{mean}) * 8.36 * (273.15 - T)^{-2.061}$$

(15)

In addition to the densification models, GEMB implements a calibration of the Arthern et al. (2010) model that was developed by Ligtenberg et al. (2011) for the Antarctic and applied by Kuipers Munneke et al. (2015) to Greenland. Using the semi-empirical model for dry snow compaction, as described by Arthern et al. (2010) in Appendix B, the *c0* and *c1* rate parameters are scaled by model-to-observed calibration values (*M0$_{550}$* for density <= 550 kg/m^3 and *M0$_{830}$* for densities between 550 kg/m^3

and 830 kg/m^3) that are trained by a comparison between firn core density profiles and modeled density profiles with respect to a climatological mean accumulation rate (C, kg m^{-2} yr^{-1}):

$$MO_{550/830} = b_{550/830} + m_{550/830} * ln(C) \qquad (16)$$

390

where 550/830 indicates coefficients for modeling of densities <= 550 kg m^{-3} and between 550 kg m^{-3} and 830 kg m^{-3}, respectively.

Offset ($b_{550/830}$) and scale ($m_{550/830}$) coefficients are estimated by spinning-up uncalibrated GEMB
395 firn profiles at node locations that are closest to the location of firn cores. Offset and scale coefficients are then determined by minimizing the least-squares fit between modeled and observed densities. These calibration coefficients are then applied in the ice sheet wide simulations.

6. Study specific model setup

6.1. Parameterization selection

400 GEMB v1.0 has many options for various model parameterizations. For this study we use a simplified version of the Gardner and Sharp (2009) albedo scheme in which albedo is modeled solely as a function of snow/ice grain specific surface area ($\hat{S}$, surface area per unit mass). Sub-surface shortwave penetration is turned off. Bare ice and shallow snow-covered ice albedo (areas with a surface density > 820 kg/m^3) are spatially varying and derived from the MODIS MCD43C3 16-day black-sky albedo
405 product (Schaaf et al, 2015). Here, we determine the bare-ice albedo by taking all summer (J,J,A) MCD43C3 16-day black-sky albedo values and calculating the lowest 10th percentile of measured albedos for every pixel. Bare ice albedos are not allowed to be less than 0.4. Albedos are then smoothed to a 0.25 degree (~32 km) resolution then bilinearly interpolated onto the GEMB model nodes. The smoothing is preformed to match the resolution of the ERA 5 climate reanalysis data, which is the
410 forcing of choice when not comparing to IAMU-FDM. The full list of selected model parameters used for this study are provided in Table 1.

6.2. Model grid

GEMB has no horizontal communication and thus easily supports non-uniform node spacing for computational efficiency, i.e. the model does not need to be run at the same spatial resolution as the
415 climate forcing. This allows the model to use a coarser node spacing for areas with small spatial gradients in surface forcing (e.g. flat ice sheet interiors) and to use refined node spacing in areas of steep spatial gradients (e.g. areas of complex topography or near ice-ocean boundaries). For the Greenland simulations presented here, we use 10990 nodes with node spacing ranging from 0.7 km along the coast to 21.1 km in the interior. For the Antarctic we simulate 50390 nodes with node spacing
420 ranging from 3.7 km along the periphery to 33.3 km in the interior. Node locations for both ice sheets are shown in Figure 2.

6.3. Atmospheric Forcing

For this study we force GEMB with climate data from the regional atmospheric climate model RACMO2.3p2 for the Antarctic (van Wessem et al., 2018) and RACMO2.3 for Greenland (Noël et al., 2015). Atmospheric fields of 10-m wind speed and 2-m temperature, surface pressure, incoming long- and short-wave radiation, vapor pressure, and precipitation are supplied at 3 hour resolution. The Antarctic product is provided at 27 km horizontal resolution for years 1979 through 2014 and Greenland data at 11 km resolution for years 1979 through 2014.

6.4. Firn model calibration

GEMB is run with the uncalibrated semi-empirical Arthern et al. (2010) firn model (Equation 12) and is forced with a repeated cycle of historical climatology until a steady-state density profile is reached, e.g. 5000 years for Greenland and 6000 years for Antarctica. The depths of the modeled density horizons are extracted at the end of this spin-up procedure, from the nodes that are closest in location to the firn cores used for calibration (Figure 3). Here we use 64 shallow firn cores and 15 deep firn cores for calibration of Greenland firn and 117 shallow and 29 deep firn cores for calibration of Antarctic firn (Montgomery et al., 2018; Smith et al., 2020; Medley et al., 2022). Firn cores are classified as shallow if they reach the beyond the 550 kg/m^3 density horizon and deep if they reach beyond the 830 kg/ m^3 density horizon. Appendix A provides the full list of cores used in the calibration and validation along with the shallow/deep classification and citation.

For these firn core locations, MO_{550} and MO_{830} are plotted independently as functions of the natural log of C (see Equation 16). A line is then fit through the points for each, representing the linear expression of how the model-to-observed depths vary as a function of C at each horizon. Next, the model steady-state spin-up is repeated, but this time multiplying the rate coefficients of $c0$ and $c1$, of the semi-empirical model of Arthern et al. (2010) (Equation 12), by MO_{550} and MO_{830}, respectively. Following Ligtenberg et al. (2011), MO_{550} and MO_{830} are allowed a minimum value of 0.25. Derived calibration offset ($b_{550/830}$) and scale ($m_{550/830}$) coefficients (Equation 16) are provided in Table 1.

The new steady-state model density profiles are then verified against the calibration subset of firn cores as well as an additional withheld subset. Figure 4 shows the modeled vs. observed 550 kg m^{-3} and 830 kg m^{-3} depths for the uncalibrated and calibrated model runs.

7. Comparison to current state-of-the-art

7.1. Surface Mass Balance

Here we compare GEMB v1.0, surface mass balance components to those computed within the RACMO surface model: RACMO2.3p2 for the Antarctic (van Wessem et al., 2018) and RACMO2.3 for Greenland (Noël et al., 2015). RACMO values are bilinear interpolated to GEMB nodes. Since both

GEMB and RACMO surfaces are forced with the same atmospheric data (RACMO), differences between modeled components can be directly attributed to differences in how surface processes are treated (e.g. albedo, roughness lengths, thermal diffusion, etc.). We also note that the RACMO surface model accounts for feedbacks between the atmosphere and the surface, while GEMB does not.

Mean spatial patterns of surface mass balance [i.e. accumulation (precipitation + deposition) – ablation (runoff + evaporation + sublimation] and Firn Air Content are shown for the Greenland in Figures 5 and 6, respectively, and for the Antarctic Ice Sheet in Figure 7. The SMB patterns for the Antarctic Ice Sheet are driven largely by snowfall and sublimation, with little contribution from meltwater runoff. In Greenland, snowfall and runoff dominate. This largely explains the much closer agreement between models in the Antarctic vs. Greenland.

In Greenland the largest differences between models are concentrated in areas of high melt and low elevation that comprise the ice sheet periphery. In general, GEMB produces more negative surface mass balance in areas of maximum melt and slightly less negative surface mass balance near the equilibrium altitude. The more negative surface mass balance at lower elevations is most likely caused by a lower "bare ice" albedo in GEMB than in RACMO. Higher surface mass balance near the equilibrium line altitude is likely due to lower rates of fresh snow melt. For the Antarctic, differences can largely be summarized as GEMB having higher rates of melt and runoff along the ice sheet periphery and lower rates of sublimation in areas conducive to katabatic winds (Parish & Bromwich, 1987). GEMB's higher rates of melt are most likely driven by lower surface albedo. Lower rates of sublimation can be attributed to the fact that GEMB does not yet (as of v1.0) include a model for snowdrift sublimation while RACMO does (Lenaerts et al., 2010).

Looking at Greenland (Figure 8) and Antarctic (Figure 9) monthly (a) and cumulative (b) time series of surface mass balance components we find very close agreement between GEMB and RACMO. Agreement is so close that several RACMO variables are not visible in the monthly time series (Figure 8a & Figure 9a) as they are overlain by near-identical GEMB output. The most notable difference is higher rates of melt for RACMO simulations in Greenland that are largely compensated for by increased meltwater retention within the firn. In the Antarctic lower rates of sublimation and higher rates of meltwater runoff in GEMB result in a slightly more positive surface mass balance trend relative to those simulated by RACMO.

7.2. Firn Air Content

Next, we compare firn properties as modeled by GEMB v1.0 to those modeled by the Institute for Marine and Atmospheric Research Utrecht Firn Densification Model (IMAU-FDM: Ligtenberg et al. 2011) run for Greenland (Ligtenberg et al. 2018) and the Antarctic (Ligtenberg et al., 2011) forced with the same RACMO data as used by the GEMB simulations (see Study specific model setup and Table 1). Like GEMB, IMAU-FDM is an uncoupled firn model (i.e. not coupled with the atmospheric model). IMAU-FDM represents the most widely used firn model results. We note that there has been a recent and rapid increase the number of ice sheet wide firn modeling studies (c.f. Brils et al., 2022; Dunmire et

al., 2021; Keenan et al., 2021; Medley et al., 2022; Veldhuijsen et al., 2022). An in-depth comparison between all modeled results would be highly valuable but is not done here. We first look at the spatial patterns of total Firn Air Content (FAC), the depth of air in meters per unit area. For Greenland, GEMB tends to generate lower FAC relative to IMAU-FDM in the West and South-East percolation zones along the ice sheet margins and a slightly higher FAC in the North East (Figure 6). This is counterintuitive as GEMB is shown to produce less melt than RACMO in areas where RACMO has a higher FAC; we would expect the opposite to be true. This difference is likely the result of a slightly more aggressive compaction calibration scaling coefficient used by GEMB (Table 1: $b_{550/830}$ = 1.27/2.00, $m_{550/830}$ = -0.12/-0.25) relative to those used by IMAU-FDM ($b_{550/830}$ = 1.04/1.73, $m_{550/830}$ = -0.09/-0.20). Differences in calibration coefficients can be attributed to differences in the firn cores used for the calibration, IMAU-FDM had access to less cores when they did their calibration, and differences in the firn models themselves.

In the Antarctic there is generally better agreement between models and scaling coefficients of $b_{550/830}$ = 1.64/2.00, $m_{550/830}$ = -0.17/-0.24 for GEMB and $b_{550/830}$ = 1.44/2.37, $m_{550/830}$ = -0.15/-0.29 for IMAU-FDM (Kuipers Munneke et al., 2015). Differences between GEMB and IMAU-FDM can be characterized as GEMB having lower FAC at low elevations and slightly higher FAC at higher elevations (Figure 7). This pattern can be attributed to GEMB having warmer surface temperatures (higher melt) at lower elevations and smaller b_{830} scaling coefficient that will impact total FAC most in areas with deep firn (i.e. the Antarctic Plateau).

It should be noted that for the runs presented here GEMB assumes an incompressible ice density of 910 kg m^{-3} while IMAU-FDM uses 917 kg m^{-3}. The overall impact on of this assumption, when comparing total FAC between models, will at worst be a 0.76% underestimate by GEMB for those columns that do not densify to ice by the time they reach the bottom of the model domain (i.e. Antarctic interior), relative to IMAU-FDM. For all other locations the difference will be significantly less.

Looking at the temporal evolution in FAC for both Greenland (Figure 8) and Antarctica (Figure 9) it can be seen that seasonal fluctuations and inter-annual variations are in very close agreement for both ice sheets but deviations in long-term trends are apparent. For the model runs examined GEMB is spun-up using the 1979-1988 climatolgy repeated for 5000 years for Greenland and the 1979-2009 climatology repeated for 6000 years for Antarctica. IMAU-FDM is spun-up using the 1960–1979 climatology repeated for as many years as it takes for the mean annual accumulation rate multiplied by the spin-up length to equal the thickness of the firn layer (from the surface to the depth at which the ice density is reached: Kuipers Munneke et al., 2015).

For Greenland (Figure 8c) GEMB has virtually no trend in FAC between 1979 and 2005, becoming more negative thereafter coincident with increases in summer melt. IMAU-FDM FAC trends positive between 1979 and 2005 after which the trend becomes negative, closely matching the rate of FAC loss simulated by GEMB. Differences in FAC trend between 1979 and 2005 can be attributed to differences

in model spin-up that are known to be a major source of uncertainty in FAC trends (Kuipers Munneke et al., 2015). Since GEMB is spun-up using the 1979-1988 clima

tology, there should be little trend in FAC over this period. GEMB was initialized to the 1979-1988 climatology as the 1960-1979 period was not included with the provided RACMO forcing. In addition, climate reanalysis are known to perform considerably better after the introduction of satellite data in 1978. This is especially true over the poles where in situ observations are sparse (Tennant, 2004). The difference in prescribed spin-up climatology between the two models is the most likely cause of the observed differences in FAC trend between 1979 and 2005. When the 1979-2005 FAC trend is removed from both products (not shown), the FAC time series are nearly identical until 2004 after which GEMB estimates ~0.5 m of FAC loss and IMAU-FDM estimates ~1.0 m of FAC loss between 2004 and 2015. Some of the difference in trend can be attributed to IMAU-FDM having higher rates of melt along the ELA during this period of time (Figure 5).

Changes in FAC for the Antarctic (Figure 9**c**) are nearly identical between models with a notable divergence beginning in 2008, after which GEMB FAC trends slightly positive and IMAU-FDM FAC trends slightly negative. Spatial patterns of FAC trends for the period pre- and post-2008 (Figure 10) show much larger rates of FAC change for the 2008-2015 period with IMAU-FDM tending to have the same sign but larger trends than GEMB. For the post 2008 period, GEMB FAC gains outcompete losses resulting in a slight positive trend in FAC over this period that is not seen in IMAU-FDM .

Despite a desire to identify which model is closer to the truth, we do not yet have an objective way to determine that. Likely the most definitive analysis will be to compare FAC corrected altimetry (e.g. ICESat/2) estimates of ice sheet mass change to mass changes derived from satellite gravimetry (i.e. GRACE/FO) data, but that is beyond the scope of this study.

8. Model sensitivity to vertical resolution

Firn and surface mass balance models are highly sensitive to the chosen setup and empirical parameterizations (Bougamont et al., 2007; Kuipers Munneke et al., 2015). Major sources of uncertainty include parameterizations of albedo, snow grain growth, surface roughness, densification and its calibration (Stevens et al., 2020), and thermal conductivity. These uncertainties become

exacerbated with the introduction of liquid water into the firn column (Vandecrux et al., 2020). Model setup can also introduce large sources of uncertainty and error. Four particularly important decisions are the choice of spin-up climatology (Kuipers Munneke et al., 2015), the length of time the spin-up is run
580 (needs to reach equilibrium to prevent model drift), and the vertical resolution of the model. Most of these sensitivities have been explored extensively and we direct the reader to previous publications that explore these topics in detail (e.g. Bougamont et al., 2007; Kuipers Munneke et al., 2015; Vandecrux et al., 2020; Stevens et al., 2020; Lundin et al., 2017).

585 One model sensitivity that we have not seen covered elsewhere is the sensitivity of the model to the vertical resolution of the firn column. The vertical resolution can have a large impact on melt rates and surface temperatures. This is because all of the energy and mass transfer between the atmosphere and the surface is often allocated to the model's uppermost layer in the firn column. A thicker layer will tend to dampen fluctuations in thermal energy relative to a thinner layer. Since snow grain growth, snow/ice
590 melt, and compaction have non-linear relations to temperature, model results will diverge for differing vertical resolutions. This is most true for the near-surface layers as thermal gradients are attenuated with depth.

To demonstrate model sensitivity to vertical resolution we run GEMB v1.0 for Greenland using the
595 same model setup (Table 1) but for four different dz_{top} [2 cm, 5 cm, 10 cm, 20 cm] and dz_{min} [1 cm, 2.5 cm, 5 cm, 10 cm] pairs (i.e., four model runs each having $dz_{min} = \frac{1}{2}\ dz_{top}$). Results of the simulations are shown in Figure 11. Increasing the size of the top layers results in a progressive reduction in melt as diurnal peak temperatures are muted and vertical gradients in temperature are reduced, in turn reducing grain metamorphism and surface darkening. Increasing the size of the top layers also results in stronger
600 thermal gradients between the atmosphere and the surface that drive larger (both positive and negative) surface latent and sensible heat and mass fluxes. This has more impact in summer when diurnal fluctuations are larger than during polar night when diurnal changes in temperature are small or non-existent. The net effect of increasing the surface layer thickness is slightly lower evaporation/sublimation losses.

605 **9. Comparison of modeled and observed near-surface temperatures**

To demonstrate the model's skill at simulating near-surface temperature, we compare GEMB v1.0 model output to an observational dataset of near-surface firn temperature that was collected at the Summit Station, Greenland (Miller et al., 2017). Here, subsurface temperatures are measured using thermistors buried within the snowpack every 20 cm, from July 2013 to June 2014. We compare these
610 observations against results produced by GEMB v1.0 forced with RACMO output (see Table 1), rerun to output concurrent daily model solutions for the location of the observations (72.580° N, 38.459° W). We correct the data for change in thermistor depth over time. By default, GEMB's thermal conductivity is calculated as a function of snow density, after Sturm et al., 1997. To investigate model sensitivity to thermal conductivity, we also run the same simulation using the density-dependent thermal conductivity
615 relation suggested by Calonne et al. (2011, Equation 12). As demonstrated by Calonne et al., 2011,

17

their solution gives a higher thermal conductivity for an equivalent density, which sits just inside of the upper bounds of the 95% confidence interval reported by Sturm et al., 1997. Here we compare results between the two GEMB simulations and the observations. For simplicity, all results are plotted with respect to the modeled or observed surface. Note that since the first thermal probe was placed at a depth of 20 cm below the surface, observational values between the snow surface and 20 cm depth are extrapolations.

Figure 12 a, c and e show the thermal profiles to a depth of 2m for observed, GEMB-Sturm and GEMB-Calonne temperatures, respectively. Figure 12 b shows the observed radiative fluxes and Figure 12 d and f show the difference between modeled and observed snow temperature profiles. Overall, there is very good agreement between the modeled and observed thermal profiles with differences resulting from errors in atmospheric forcing, errors in observations, and biases attributed to errors in model parameterizations. Both model simulations produce mean temperatures between 0.2 and 2 meters depth that are ~0.8 K warmer than the observations, with the Sturm parameterization of thermal conductivity producing slightly better agreement (0.77 K) than the Calonne parameterization (0.79 K). Looking at bias and root-mean-square error as a function of depth, it can be seen (Figure 13) that the Sturm parameterization produces slightly better agreement to the observations in the top 0.5 meters of the snow pack while the Calonne parameterization produces significantly better fit for depths below 0.8 meters. From this single location comparison, the Calonne parameterization outperforms the Sturm parametrization. Drawing any more definitive conclusions is challenging given other sources of disagreement such as atmospheric forcing and density structure.

While differences in mean temperature are only ~0.8 K, seasonal differences can be as large as 5 K (Figure 13). A 5 K increase in snow/firn temperature increases the compaction rate by a factor of 1.6-1.8. Since compaction rates are strongly dependent on temperature, seasonal biases in temperate have a large impact on rates of firn compaction, even if annual biases are small. Therefore future work should prioritize improving near-surface atmospheric temperatures over glacier surface and thermal diffusion within snow and ice.

Calonne et al. (2019) show that the quadric relations between effective thermal conductivity and density, that are often used for snow (e.g. Equation 4 & 5), do not perform well for firn and porous ice. Instead, they propose an alternative empirical relation to more accurately model effective conductivity for the full range of densities from 0 to 917 kg m^{-3} (see Equation 5 in Calonne et al., 2019). We plan to include empirical relations proposed by Calonne et al. (2019) in a future version of GEMB.

10. Summary and Conclusions

This paper provides the first description of version 1.0 of the open-source Glacier Energy and Mass Balance (GEMB) model that has been integrated as a module into the Ice-sheet and Sea-level System Model (ISSM). The model is one-way coupled with the atmosphere which allows it to be run off-line

655 with a diversity of climate forcing but neglects feedback to the atmosphere. GEMB is written in C++ which produces efficient compiled machine code for fast execution. GEMB provides numerous parameterization choices for various key processes (e.g. albedo, subsurface shortwave absorption, and compaction), making it well suited for uncertainty quantification and model exploration.

660 To evaluate output from GEMB we compare it to the model output from the Institute for Marine and Atmospheric Research Utrecht Firn Densification Model (IMAU-FDM: Ligtenberg et al. 2011) for both Greenland (Ligtenberg et al. 2018) and the Antarctic (Ligtenberg et al., 2011). Models are forced with the same RACMO climate data (see Study specific model setup: Table 1) and are independently calibrated to ice core density profiles. By forcing GEMB with the same climate data as IMAU-FDM we
665 are able to attribute differences in model output to differences in model parameterizations and setup.

Overall, we find good agreement between models for both ice sheets with a few notable differences. For Greenland GEMB produces considerably less melt than IMAU-FDM but nearly as much runoff. This is because, relative to IMAU-FDM, GEMB tends to generate more low elevation melt that runs off and
670 less high elevation melt that refreezes within the firn. These differences are most likely due to inter-model differences in the bare ice albedo and fresh snow melt. GEMB and IMAU-FDM produce considerably different trends in FAC that are the result of differing climatologies used for model spin-up. GEMB used the 1979-1988 climatology repeated for 5000 years while IMAU-FDM used the 1960-1979 climatology. This results in GEMB having little trend in FAC prior to the onset of increased
675 melting in 2005. In contrast, IMAU-FDM has a positive FAC trend from 1979-2005 and a negative trend thereafter. These differences can have a large impact on volume-to-mass conversions used to generate glacier mass change estimates from satellite altimetry. For the Antarctic, GEMB and IMAU-IMAU-FDM are nearly identical with GEMB having slightly lower rates of sublimation and slightly higher rates of meltwater runoff that lead to a slightly more positive surface mass balance trend than
680 found in IMAU-FDM. Changes in FAC for the Antarctic are nearly identical between models with a notable divergence beginning in 2008, after which GEMB FAC trends slightly positive and IMAU-FDM FAC trends slightly negative.

To demonstrate the impact of model setup we explore the impact of the model's vertical resolution on
685 the results. We show that increasing the model's vertical resolution decreases melt and increases surface latent and sensible heat fluxes due to stronger thermal gradients between the surface and the atmosphere. Lastly, we compare modeled near-surface thermal profiles, calculated using two different density-thermal conductivity relations, to in situ observations collected at Summit Station, Greenland. Our comparison shows good agreement between modeled and observed temperatures, with slightly
690 improved agreement using the Calonne versus the Sturm thermal conductivity parameterization.

Our analysis shows that the GEMB model performs as expected and produces results that are comparable to an existing state-of-the-art firn model (IMAU-FDM). There are notable differences in output between the models but it is difficult to judge if one model outperforms the other as there is
695 insufficient observational data to distinguish between models. Future studies that compare altimetry

19

derived mass changes, with those derived from satellite gravimetry should help to distinguish between models.

Future work will focus on developing atmospheric and firn downscaling routines that will allow GEMB
700 to produce higher resolution output when forced with medium resolution (30-100 km) climate reanalysis or coarse resolution (200-500 km) climate model output.

Code availability:
GEMB is a module implemented inside of ISSM. The archived version of the source code used in this
705 paper is made available as part of a Zenodo repository at https://doi.org/10.5281/zenodo.7026445 (ISSM team, 2022) code can be downloaded, compiled, and executed following the instructions available on the ISSM website: https://issm.jpl.nasa.gov/download (last access: August 26, 2022). The public SVN repository for the ISSM code can also be found directly at https://issm.ess.uci.edu/svn/issm/issm/trunk, and can be downloaded using username "anon" and
710 password "anon". The version of the code for this study, corresponding to ISSM release 4.21, is SVN version tag number 27238. An unmaintained MATLAB version of the model is also available (Gardner, A. S., 2022). It is recommended to use the well maintained ISSM version of GEMB.

Data availability:
715 All GEMB and RACMO/IMAU-FDM model output used to generate Figures 2 through 13 and Appendix A can be found in Schlegel, N-J. et al. (2022).

Author contribution:
A.G. wrote the model, co-wrote the paper, and made the figures. N.S. ran all of the experiments and co-
720 wrote the paper. E.L. translated the original model from Matlab into C++ and integrated it into ISSM.

Competing interests:
The authors declare that they have no competing interests.

References

Alexander, P. M., Tedesco, M., Fettweis, X., van de Wal, R. S. W., Smeets, C. J. P. P., and van den Broeke, M. R., 2014: Assessing spatio-temporal variability and trends in modelled and measured Greenland Ice Sheet albedo (2000–2013), The Cryosphere, 8, 2293–2312, https://doi.org/10.5194/tc-8-2293-2014.

740   Alley, R. B. (1987). Firn densification by grain-boundary sliding: a first model. Le Journal de Physique Colloques, 48(C1), C1-249.

Arthern, R. J., Vaughan, D.G., Rankin, A.M., Mulvaney, R, and Thomas, E.R., 2010: In situ measurements of Antarctic snow compaction compared with predictions of models, J. Geophys. Res., 115, F03011, doi:10.1029/2009JF001306.

745   Arthern, R. J., & Wingham, D. J. (1998). The Natural Fluctuations of Firn Densification and Their Effect on the Geodetic Determination of Ice Sheet Mass Balance. Climatic Change, 40(3), 605–624. https://doi.org/10.1023/A:1005320713306

Bartelt, P., & Lehning, M. (2002). A physical SNOWPACK model for the Swiss avalanche warning Part I: Numerical model. Cold Regions Science and Technology, 35(3), 123–145.
750   file:///E:/Work_Computer/Articles/Articles/Bartelt, 2002. Cold Regions Sci %26 Tech. v35.pdf

Bassford, R. P., 2002: Geophysical and numerical modelling investigations of the ice caps in Severnaya Zemlya. Ph.D. thesis, University of Bristol, England.

Bassford, R. P., M. J. Siegert, J. A. Dowdeswell, J. Oerlemans, A. F. Glazovsky & Y. Y. Macheret (2006) Quantifying the Mass Balance of Ice Caps on Severnaya Zemlya, Russian High Arctic. I:
755   Climate and Mass Balance of the Vavilov Ice Cap, Arctic, Antarctic, and Alpine Research, 38:1, 1-12, DOI: 10.1657/1523-0430(2006)038[0001:QTMBOI]2.0.CO;2

Beljaars, A. C. M., & Holtslag, A. A. M. (1991). Flux parameterization over land surfaces for atmospheric models. Journal of Applied Meteorology, 30(3), 327–341.

Bolton, D. (1980). The computation of equivalent potential temperature. Monthly Weather Review,
760   108, 1046–1953.

Bougamont, M., & Bamber, J. L. (2005). A surface mass balance model for the Greenland Ice Sheet. Journal of Geophysical Research-Earth Surface, 110(F4), doi:10.1029/2005JF000348.

Bougamont, M., Bamber, J. L., Ridley, J. K., Gladstone, R. M., Greuell, W., Hanna, E., Payne, A. J., & Rutt, I. (2007). Impact of model physics on estimating the surface mass balance of the Greenland Ice
765   Sheet. Geophysical Research Letters, 34(17), doi:10.1029/2007GL030700. http://internal-pdf//Bougamont, 2007. GRL. v34-1931089158/Bougamont, 2007. GRL. v34.pdf

Brils, M., Kuipers Munneke, P., van de Berg, W. J., & van den Broeke, M. (2022). Improved representation of the contemporary Greenland ice sheet firn layer by IMAU-FDM v1.2G. *Geosci. Model Dev.*, *15*(18), 7121–7138. https://doi.org/10.5194/gmd-15-7121-2022

770   Brun, E., (1989). Investigation on wet-snow metamorphism in respect of liquid-water content. Annals of Glaciology, 13, 22-26.

Brun, E., P. David, M. Sudul, and G. Brunot, (1992). A numerical model to simulate snow-cover stratigraphy for operational avalanche forecasting. Journal of Glaciology, 38, 13-22.

Brun, E., Martin, E., Simon, V., Gendre, C., & Coleou, C. (1989). An energy and mass model of snow cover suitable for operational avalanche forecasting. Journal of Glaciology, 35(121), 333–342. file:///E:/Work_Computer/Articles/Articles/Brun, 1989. J Glaciology. v35.pdf

Calonne, N., Milliancourt, L., Burr, A., Philip, A., Martin, C. L., Flin, F., & Geindreau, C. (2019). Thermal Conductivity of Snow, Firn, and Porous Ice From 3-D Image-Based Computations. Geophysical Research Letters, 46(22), 13079–13089. https://doi.org/https://doi.org/10.1029/2019GL085228

Calonne, N., Flin, F., Morin, S., Lesaffre, B., du Roscoat, S. Rolland, and Geindreau, C. (2011), Numerical and experimental investigations of the effective thermal conductivity of snow, Geophys. Res. Lett., 38, L23501, doi:10.1029/2011GL049234.

Colbeck, S. C. (1982). An overview of seasonal snow metamorphism. Reviews of Geophysics and Space Physics, 20(1), 45–61. file:///E:/Work_Computer/Articles/Articles/Colbeck, 1982. Reviews of Geophysics and Space Physics. v20.pdf

Colbeck, S. C. (1974). The capillary effects on water percolation in homogeneous snow. *Journal of Glaciology*, *13*(67), 85–97. https://doi.org/DOI: 10.3189/S002214300002339X

Coléou, C., & Lesaffre, B. (1998). Irreducible water saturation in snow: experimental results in a cold laboratory. Annals of Glaciology, 26, 64–68. https://doi.org/DOI: 10.3189/1998AoG26-1-64-68

Copernicus Climate Change Service (C3S): ERA5: Fifth generation of ECMWF atmospheric reanalyses of the global climate . Copernicus Climate Change Service Climate Data Store (CDS), date of access: Jan 25, 2019. https://cds.climate.copernicus.eu/cdsapp#!/home, 2017

Courant, R., Friedrichs, K., & Lewy, H. (1928). Über die partiellen Differenzengleichungen der mathematischen Physik. Mathematische Annalen, 100(1), 32–74.

Ding, M., Yang, D., van den Broeke, M., Allison, I., Xiao, C., Qin, D., & Huai, B. (2020). The surface energy balance at Panda 1 Station, Princess Elizabeth Land: A typical katabatic wind region in East Antarctica. Journal of Geophysical Research: Atmospheres, 125, e2019JD030378. https://doi.org/10.1029/2019JD030378.

Culberg, R., Schroeder, D. M., and Chu, W.: Extreme melt season ice layers reduce firn permeability across Greenland, Nature communications, 12, 1, 1-9, 2021.

Fausto, R. S., Box, J. E., Vandecrux, B., van As, D., Steffen, K., MacFerrin, M., Machguth, H., Colgan, W., Koenig, L. S., McGrath, D., Charalampidis, C., & Braithwaite, R. J. (2018). A snow density dataset for improving surface boundary conditions in Greenland ice sheet firn modelling. *Frontiers in Earth Science*, 6(51). https://doi.org/10.3389/feart.2018.00051

Flanner, M. G., & Zender, C. S. (2006). Linking snowpack microphysics and albedo evolution. Journal of Geophysical Research-Atmospheres, 111(D12208), doi:10.1029/2005JD006834. http://internal-pdf//Flanner, 2006. JGR. v111-4182110721/Flanner, 2006. JGR. v111.pdf

22

Foken T. (2008). Micrometeorology . Berlin: Springer.

810 Forster, R. R., Box, J. E., van den Broeke, M. R., Miège, C., Burgess, E. W., van Angelen, J. H., Lenaerts, J. T. M., Koenig, L. S., Paden, J., Lewis, C., Gogineni, S. P., Leuschen, C., & McConnell, J. R. (2014). Extensive liquid meltwater storage in firn within the Greenland ice sheet. Nature Geoscience, 7(2), 95–98. https://doi.org/10.1038/ngeo2043

Gardner, A. S. and M. J. Sharp, 2010: A review of snow and ice albedo and the development of a new 815 physically based broadband albedo parameterization. Journal of geophysical research, 115 (F1), F01 009.

Gardner, A. S. (2022). Glacier Energy and Mass Balance - MATLAB (v0.1). Zenodo. https://doi.org/10.5281/zenodo.6975252

Greuell, W., and Konzelmann, T., 1994: Numerical modelling of the energy balance and the englacial 820 temperature of the Greenland Ice Sheet. Calculations for the ETH-Camp location (West Greenland, 1155 m a.s.l.). Global and Planetary Change, 9: 91–114.

Greuell, W., & Oerlemans, J. (1989). The Evolution of the Englacial Temperature Distribution in the Superimposed Ice Zone of a Polar Ice Cap During a Summer Season BT - Glacier Fluctuations and Climatic Change (J. Oerlemans (Ed.); pp. 289–303). Springer Netherlands.

825 Guyomarc'h, G. and Merindol, L. (1998) Validation of an application for forecasting blowing snow, Ann. Glaciol., 26, 138–143.

Helsen, M. M., M. R. van den Broeke, R. S. W. van de Wal, W. J. van de Berg, E. van Meijgaard, C. H. Davis, Y. Li, and I. Goodwin, 2008: Elevation changes in Antarctica mainly determined by accumulation variability, Science, 320, 1626– 1629, doi:10.1126/science.1153894.

830 Herron, M., and Langway, C. (1980). Firn Densification: An Empirical Model. Journal of Glaciology, 25(93), 373-385. doi:10.3189/S0022143000015239.

Hirashima, H., Avanzi, F., & Yamaguchi, S. (2017). Liquid water infiltration into a layered snowpack: evaluation of a 3-D water transport model with laboratory experiments. Hydrol. Earth Syst. Sci., 21(11), 5503–5515. https://doi.org/10.5194/hess-21-5503-2017

835 Högström U. (1996). Review of some basic characteristics of the atmospheric surface layer. Boundary-Layer Meteorology 78,215246.

Horlings, A. N., Christianson, K., Holschuh, N., Stevens, C. M., & Waddington, E. D. (2021). Effect of horizontal divergence on estimates of firn-air content. Journal of Glaciology, 67(262), 287–296. https://doi.org/DOI: 10.1017/jog.2020.105

840 ISSM Team. (2022). Ice-sheet and Sea-level System Model source code, v4.21 r27238 (4.21). Zenodo. https://doi.org/10.5281/zenodo.7026445

Janssens, I., & Huybrechts, P. (2000). The treatment of meltwater retention in mass-balance parameterizations of the Greenland ice sheet. Annals of Glaciology, 31, 133–140. https://doi.org/DOI: 10.3189/172756400781819941

845 Kaspers, K. A., van de Wal, R. S. W., van den Broeke, M. R., Schwander, J., van Lipzig, N. P. M., and Brenninkmeijer, C. A. M.: Model calculations of the age of firn air across the Antarctic continent, Atmos. Chem. Phys., 4, 1365–1380, https://doi.org/10.5194/acp-4-1365-2004, 2004.

Keenan, E., Wever, N., Dattler, M., Lenaerts, J. T. M., Medley, B., Kuipers Munneke, P., & Reijmer, C. (2021). Physics-based SNOWPACK model improves representation of near-surface Antarctic snow and
850 firn density. *The Cryosphere*, *15*(2), 1065–1085. https://doi.org/10.5194/tc-15-1065-2021

Kuipers Munneke, P., Ligtenberg, S. R. M., Noël, B. P. Y., Howat, I. M., Box, J. E., Mosley-Thompson, E., McConnell, J. R., Steffen, K., Harper, J. T., Das, S. B., and van den Broeke, M. R., 2015: Elevation change of the Greenland Ice Sheet due to surface mass balance and firn processes, 1960–2014, The Cryosphere, 9, 2009–2025, https://doi.org/10.5194/tc-9-2009-2015.

855 Larour, E., M. Morlighem, H. Seroussi, J. Schiermeier and E. Rignot, 2012a, Ice flow sensitivity to geothermal heat flux of Pine Island Glacier, Antarctica, J. Geophys. Res., 117, F04023, doi:10.1029/2012JF002371.

Larour, E., J. Schiermeier, E. Rignot, H. Seroussi, and M. Morlighem, 2012b, Sensitivity Analysis of Pine Island Glacier ice flow using ISSM and DAKOTA, J. Geophys. Res., 117, F02009,
860 doi:10.1029/2011JF002146.

Lefebre, F., H. Galle´e, J.-P. van Ypersele, and W. Greuell, 2003: Modeling of snow and ice melt at ETH Camp (West Greenland): A study of surface albedo, J. Geophys. Res., 108(D8), 4231, doi:10.1029/2001JD001160.

Lenaerts, J. T. M., van den Broeke, M. R., Déry, S. J., König-Langlo, G., Ettema, J., & Munneke, P. K.
865 (2010). Modelling snowdrift sublimation on an Antarctic ice shelf. The Cryosphere, 4(2), 179–190. https://doi.org/10.5194/tc-4-179-2010,

Li, J., & Zwally, H., 2004: Modeling the density variation in the shallow firn layer. *Annals of Glaciology, 38*, 309-313. doi:10.3189/172756404781814988.

Ligtenberg, S. R. M., Helsen, M. M., and van den Broeke, M. R., 2011: An improved semi-empirical
870 model for the densification of Antarctic firn. The Cryosphere, 5(4), 809–819. https://doi.org/10.5194/tc-5-809-2011
Ligtenberg, S. R. M., Kuipers Munneke, P., Noël, B. P. Y., and van den Broeke, M. R.: Brief communication: Improved simulation of the present-day Greenland firn layer (1960–2016), The Cryosphere, 12, 1643–1649, https://doi.org/10.5194/tc-12-1643-2018, 2018.

875 Liston, G. E., & Elder, K. (2006). A Distributed Snow-Evolution Modeling System (SnowModel). Journal of Hydrometeorology, 7(6), 1259–1276. https://doi.org/10.1175/JHM548.1

Lundin, J. M. D., Stevens, C. M., Arthern, R., Buizert, C., Orsi, A., Ligtenberg, S. R. M., Simonsen, S. B., Cummings, E., Essery, R., Leahy, W., Harris, P., Helsen, M. M., & Waddington, E. D. (2017). Firn Model Intercomparison Experiment (FirnMICE). Journal of Glaciology, 63(239), 401–422.
880 https://doi.org/10.1017/jog.2016.114

MacFerrin, M., Machguth, H., van As, D., Charalampidis, C., Stevens, C. M., Heilig, A., Vandecrux B., et al.: Rapid expansion of Greenland's low-permeability ice slabs, Nature 573, 7774, 403-407, 2019

24

Marbouty, D., 1980: An experimental study of temperature-gradient metamorphism. Journal of Glaciology, 26, 303-312.

885 Male, D. H., & Granger, R. J. (1981). Snow surface energy exchange. Water Resources Research, 17(3), 609–627. file:///E:/Work_Computer/Articles/Articles/Male, 1981. Water Resources Research. V17.pdf

Marsh, P., & Woo, M.K. (1984). Wetting front advance and freezing of meltwater within a snow cover: 2. A simulation model. Water Resources Research, 20(12), 1865–1874.
890 https://doi.org/https://doi.org/10.1029/WR020i012p01865

Marchenko, S., van Pelt, W. J. J., Claremar, B., Pohjola, V., Pettersson, R., Machguth, H., & Reijmer, C. (2017). Parameterizing Deep Water Percolation Improves Subsurface Temperature Simulations by a Multilayer Firn Model . In Frontiers in Earth Science (Vol. 5, p. 16). https://www.frontiersin.org/article/10.3389/feart.2017.00016

895 Medley, B., Neumann, T. A., Zwally, H. J., Smith, B. E., & Stevens, C. M. (2022). Simulations of firn processes over the Greenland and Antarctic ice sheets: 1980–2021. *The Cryosphere*, *16*(10), 3971–4011. https://doi.org/10.5194/tc-16-3971-2022

Miller, J. Z., Culberg, R., Long, D. G., Shuman, C. A., Schroeder, D. M., and Brodzik, M. J.: An empirical algorithm to map perennial firn aquifers and ice slabs within the Greenland Ice Sheet using
900 satellite L-band microwave radiometry, The Cryosphere, 16, 103–125, https://doi.org/10.5194/tc-16-103-2022, 2022.

Miller, N. B., Shupe, M. D., Cox, C. J., Noone, D., Persson, P. O. G., and Steffen, K.: Surface energy budget responses to radiative forcing at Summit, Greenland, The Cryosphere, 11, 497–516, https://doi.org/10.5194/tc-11-497-2017, 2017.

905 Montgomery, L., L. Koenig, and P. Alexander, 2018: The SUMup dataset: Compiled measurements of surface mass balance components over ice sheets and sea ice with analysis over Greenland. Earth Syst. Sci. Data, 10, 1959-1985, doi:10.5194/essd-10-1959-2018.

Munro, D. S., & Davies, J. A. (1977). An experimental study of the glacier boundary layer over melting ice. Journal of Glaciology, 18(80), 425–436. https://doi.org/DOI: 10.3189/S0022143000021109

910 Murphy, D.M. and Koop, T., 2005: Review of the Vapour Pressures of Ice and Supercooled Water for Atmospheric Applications. Quarterly Journal of the Royal Meteorological Society, 131, 1539-1565. http://dx.doi.org/10.1256/qj.04.94

Murray, F. W. (1967). "On the Computation of Saturation Vapor Pressure." *J. Appl. Meteor.* 6 (1): 203–4. https://doi.org/10.1175/1520-0450(1967)006%3C0203:OTCOSV%3E2.0.CO;2.

915 Noël, B., van de Berg, W. J., Machguth, H., Lhermitte, S., Howat, I., Fettweis, X., & van den Broeke, M. R. (2016). A daily, 1 km resolution data set of downscaled Greenland ice sheet surface mass balance (1958–2015). The Cryosphere, 10(5), 2361–2377. https://doi.org/10.5194/tc-10-2361-2016

Paterson, W., 1994: The Physics of Glaciers, 3rd ed., Pergamon Press, Oxford, London, New York.

Parish, T. R., & Bromwich, D. H. (1987). The surface windfield over the Antarctic ice sheets. *Nature*, 920 *328*(6125), 51–54. https://doi.org/10.1038/328051a0

Patankar, S. V. (1980). *Numerical Heat Transfer and Fluid Flow*. Hemisphere Publishing Corp.

Pfeffer, W. T., Illangasekare, T. H., & Meier, M. F. (1990). Analysis and Modeling of Melt-Water Refreezing in Dry Snow. Journal of Glaciology, 36(123), 238–246. https://doi.org/DOI: 10.3189/S0022143000009497

925 Pfeffer, W. T., Meier, M. F., & Illangasekare, T. H. (1991). Retention of Greenland Runoff by Refreezing - Implications for Projected Future Sea-Level Change. Journal of Geophysical Research-Oceans, 96(C12), 22117–22124. http://internal-pdf//Pfeffer, 1991. JGR. v96-1317438466/Pfeffer, 1991. JGR. v96.pdf

Schlegel, N-J, E Larour, H Seroussi, M. Morlighem, and J. E. Box, 2013, Decadal-scale sensitivity of 930 northeast Greenland ice flow to errors in surface mass balance using ISSM J. Geophys. Res. - Earth Surface, 118, doi: 10.1002/jgrf.20062.

Schlegel, N.-J., E. Larour, H. Seroussi, M. Morlighem and J.E. Box, 2015, Ice discharge uncertainties in Northeast Greenland from boundary conditions and climate forcing of an ice flow model, J. Geophys. Res., 120, 29-54, doi:10.1002/2014JF003359.

935 Schlegel, N-J. and E. Y. Larour, 2019, Quantification of surface forcing requirements for a Greenland Ice Sheet model using uncertainty analyses. Geophys. Res. Lett., 46. https://doi.org/10.1029/2019GL083532.

Schlegel, Nicole-Jeanne, Gardner, Alex, & Larour, Eric. (2022). Output from the Glacier Energy and Mass Balance (GEMB v1.0) forced with 3-hourly RACMO fields, Greenland and Antarctica 1979-2014 940 (1.1) [Data set]. Zenodo. https://doi.org/10.5281/zenodo.7430469

Schaaf, C., Z. Wang. *MCD43C3 MODIS/Terra+Aqua BRDF/Albedo Albedo Daily L3 Global 0.05Deg CMG V006*. 2015, distributed by NASA EOSDIS Land Processes DAAC, https://doi.org/10.5067/MODIS/MCD43C3.006. Accessed 2020-03-19.

945 Smith B, Fricker HA, Gardner AS, Medley B, Nilsson J, Paolo FS, Holschuh N, Adusumilli S, Brunt K, Csatho B, Harbeck K, Markus T, Neumann T, Siegfried MR, Zwally HJ, 2020: Pervasive ice sheet mass loss reflects competing ocean and atmosphere processes. Science. 2020 Jun 12;368(6496):1239-1242. doi: 10.1126/science.aaz5845. Epub 2020 Apr 30. PMID: 32354841.

Sjöblom, A. (2014). Turbulent fluxes of momentum and heat over land in the High-Arctic summer: the 950 influence of observation techniques. *Polar Research*, *33*. https://doi.org/10.3402/polar.v33.21567

Steger, C. R., Reijmer, C. H., van den Broeke, M. R., Wever, N., Forster, R. R., Koenig, L. S., Kuipers Munneke, P., Lehning, M., Lhermitte, S., Ligtenberg, S. R. M., Miège, C., & Noël, B. P. Y. (2017). Firn Meltwater Retention on the Greenland Ice Sheet: A Model Comparison . In Frontiers in Earth Science (Vol. 5, p. 3). https://www.frontiersin.org/article/10.3389/feart.2017.00003

955   Stevens, C. M., Verjans, V., Lundin, J. M. D., Kahle, E. C., Horlings, A. N., Horlings, B. I., & Waddington, E. D. (2020). The Community Firn Model (CFM) v1.0. Geosci. Model Dev., 13(9), 4355–4377. https://doi.org/10.5194/gmd-13-4355-2020

Sturm, M., J. Holmgren, M. König, and K. Morris, 1997: The thermal conductivity of seasonal snow, J. Glaciol., 43, 26–41.

960   Tennant, W. (2004). Considerations when using pre-1979 NCEP/NCAR reanalyses in the southern hemisphere. Geophysical Research Letters, 31(11). https://doi.org/https://doi.org/10.1029/2004GL019751

van Angelen, J. H., Lenaerts, J. T. M., van den Broeke, M. R., Fettweis, X., & van Meijgaard, E. (2013). Rapid loss of firn pore space accelerates 21st century Greenland mass loss. Geophysical
965   Research Letters, n/a-n/a. https://doi.org/10.1002/grl.50490

van den Broeke, M. R., Duynkerke, P. G., & Henneken, E. A. C. (1994). Heat, momentum and moisture budgets of the katabatic layer over the melting zone of the West Greenland Ice Sheet in summer. Boundary-Layer Meteorology, 71(4), 393–413.

Vandecrux, B., Mottram, R., Langen, P. L., Fausto, R. S., Olesen, M., Stevens, C. M., Verjans, V.,
970   Leeson, A., Ligtenberg, S., Kuipers Munneke, P., Marchenko, S., van Pelt, W., Meyer, C. R., Simonsen, S. B., Heilig, A., Samimi, S., Marshall, S., Machguth, H., MacFerrin, M., … Box, J. E. (2020). The firn meltwater Retention Model Intercomparison Project (RetMIP): evaluation of nine firn models at four weather station sites on the Greenland ice sheet. The Cryosphere, 14(11), 3785–3810. https://doi.org/10.5194/tc-14-3785-2020

975   van Wessem, J. M., van de Berg, W. J., Noël, B. P. Y., van Meijgaard, E., Amory, C., Birnbaum, G., Jakobs, C. L., Krüger, K., Lenaerts, J. T. M., Lhermitte, S., Ligtenberg, S. R. M., Medley, B., Reijmer, C. H., van Tricht, K., Trusel, L. D., van Ulft, L. H., Wouters, B., Wuite, J., and van den Broeke, M. R. 2018: Modelling the climate and surface mass balance of polar ice sheets using RACMO2 – Part 2: Antarctica (1979–2016), The Cryosphere, 12, 1479–1498, https://doi.org/10.5194/tc-12-1479-2018.

980   Vandecrux, B., MacFerrin, M., Machguth, H., Colgan, W. T., van As, D., Heilig, A., Stevens, C. M., Charalampidis, C., Fausto, R. S., Morris, E. M., Mosley-Thompson, E., Koenig, L., Montgomery, L. N., Miège, C., Simonsen, S. B., Ingeman-Nielsen, T., & Box, J. E. (2019). Firn data compilation reveals widespread decrease of firn air content in western Greenland. The Cryosphere, 13(3), 845–859. https://doi.org/10.5194/tc-13-845-2019

985   Van Der Veen, C. J. (1993). Interpretation of short-term ice-sheet elevation changes inferred from satellite altimetry. Climatic Change, 23(4), 383–405. https://doi.org/10.1007/BF01091624

Veldhuijsen, S. B. M., van de Berg, W. J., Brils, M., Kuipers Munneke, P., & van den Broeke, M. R. (2022). Characteristics of the contemporary Antarctic firn layer simulated with IMAU-FDM v1.2A (1979-2020). *The Cryosphere Discuss.*, *2022*, 1–26. https://doi.org/10.5194/tc-2022-118

990   Vionnet, V., Brun, E., Morin, S., Boone, A., Faroux, S., Le Moigne, P., Martin, E., and Willemet, J.-M., 2012: The detailed snowpack scheme Crocus and its implementation in SURFEX v7.2, Geosci. Model Dev., 5, 773–791, https://doi.org/10.5194/gmd-5-773-2012.

Warren, S. G., & Wiscombe, W. J. (1980). A model for the spectral albedo of snow. II: Snow containing atmospheric aerosols. Journal of the Atmospheric Sciences, 37(12), 2734–2745. 1980. J.
995   Atmospheric Sciences. v37.pdf

Weinhart, A. H., Freitag, J., Hörhold, M., Kipfstuhl, S., and Eisen, O.: Representative surface snow density on the East Antarctic Plateau, The Cryosphere, 14, 3663–3685, https://doi.org/10.5194/tc-14-3663-2020, 2020.

Wiscombe, W. J., & Warren, S. G. (1980). A model for the spectral albedo of snow. I: Pure snow.
000   Journal of the Atmospheric Sciences, 37(12), 2712–2733. file:///E:/Work_Computer/Articles/Articles/Wiscombe, 1980. J. Atmospheric Sciences. V37.pdf

Zwally, H. J. A. Y., Bindschadler, R. A., Brenner, A. C., Major, J. A., & Marsh, J. G. (1989). Growth of Greenland Ice Sheet: Measurement. Science, 246(4937), 1587 LP – 1589. https://doi.org/10.1126/science.246.4937.1587

005   Zwally, H. J., Giovinetto, M. B., Li, J., Cornejo, H. G., Beckley, M. A., Brenner, A. C., Saba, J. L., & Yi, D. (2005). Mass changes of the Greenland and Antarctic ice sheets and shelves and contributions to sea-level rise: 1992–2002. Journal of Glaciology, 51(175), 509–527. https://doi.org/DOI: 10.3189/172756505781829007

010 **Tables**

Table 1: GEMB model parameters used in this study

Parameter	Greenland	Antarctic
dz_{top}	0.05 m	0.05 m
dz_{min}	0.025 m	0.025 m
z_{top}	10 m	10 m
z_{max}	250 m	250 m
z_{min}	130 m	130 m
Thermal conductivity	Strum et al., 1997	Strum, 1997
Albedo	Gardner and Sharp, 2009 $d\alpha_c$, $d\alpha_u$, $d\alpha_\tau$ set to zero	Gardner and Sharp, 2009 $d\alpha_c$, $d\alpha_u$, $d\alpha_\tau$ set to zero
Bare ice albedo	MODIS MCD43C3	MODIS MCD43C3
SW subsurface absorption	No	No
Compaction	Arthern et al. (2010)	Arthern et al. (2010)
Compaction calibration	Kuipers Munneke et al. (2015) $b_{550/830} = 1.27/2.00$ $m_{550/830} = -0.12/-0.25$ $r^2_{550/830} = 0.18/0.92$	Ligtenberg et al. (2011) $b_{550/830} = 1.64/2.00$ $m_{550/830} = -0.17/-0.24$ $r^2_{550/830} = 0.28/0.55$
Falling snow density	315 kg/m^3 (Fausto et al., 2018)	function of the annual temperature, accumulation, surface pressure and wind speed (Kaspers et al. 2004)
Spinup	~5000 years Climatology 1979-1988	~6000 years Climatology 1979-2009

Figures
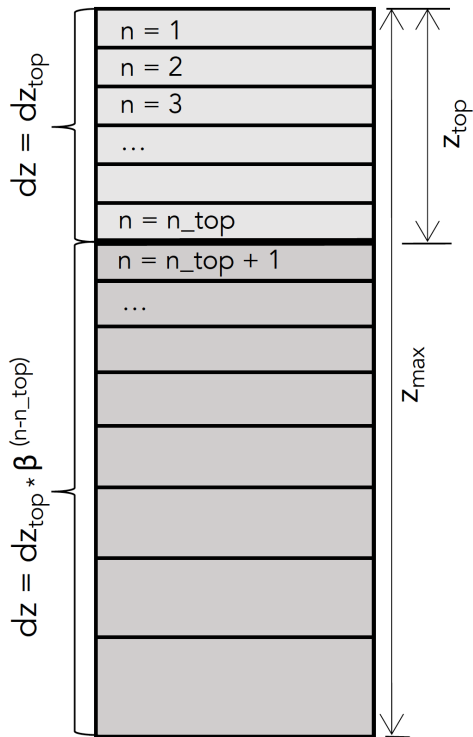
015

Figure 1: Diagram showing the model layer initialization as described in Section 2.1. *dz* is the layer thickness, *dz_{top}* is the maximum near-surface layer thickness, *z_{top}* is the depth of the near-surface, *z_{max}* is the maximum column depth, *β* is a unitless scaling by depth parameter, and *n* is the layer number.
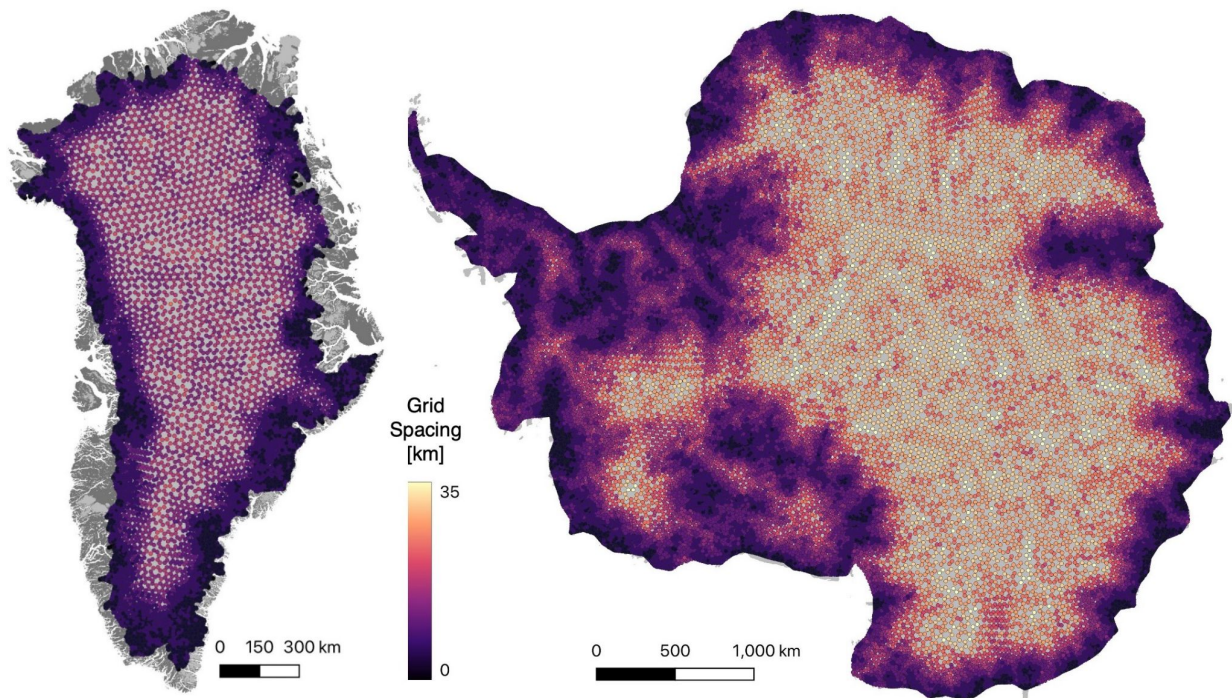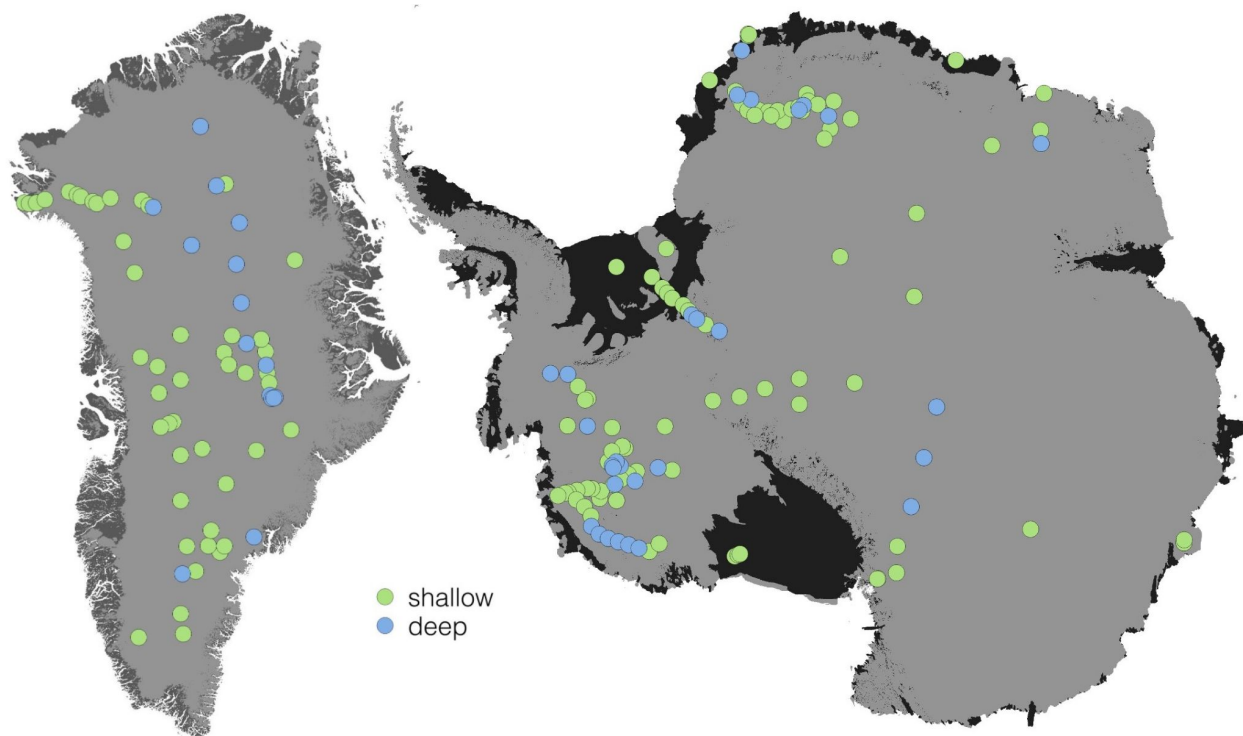
020

Figure 2: GEMB Greenland (left) and Antarctic (right) model node locations used for this study.

31

025

Figure 3: Locations of shallow (green) and deep (blue) firn cores. Firn cores are classified as shallow if they reach the 550 kg m^{-3} density horizon and deep if they extend to the 830 kg m^{-3} density horizon.
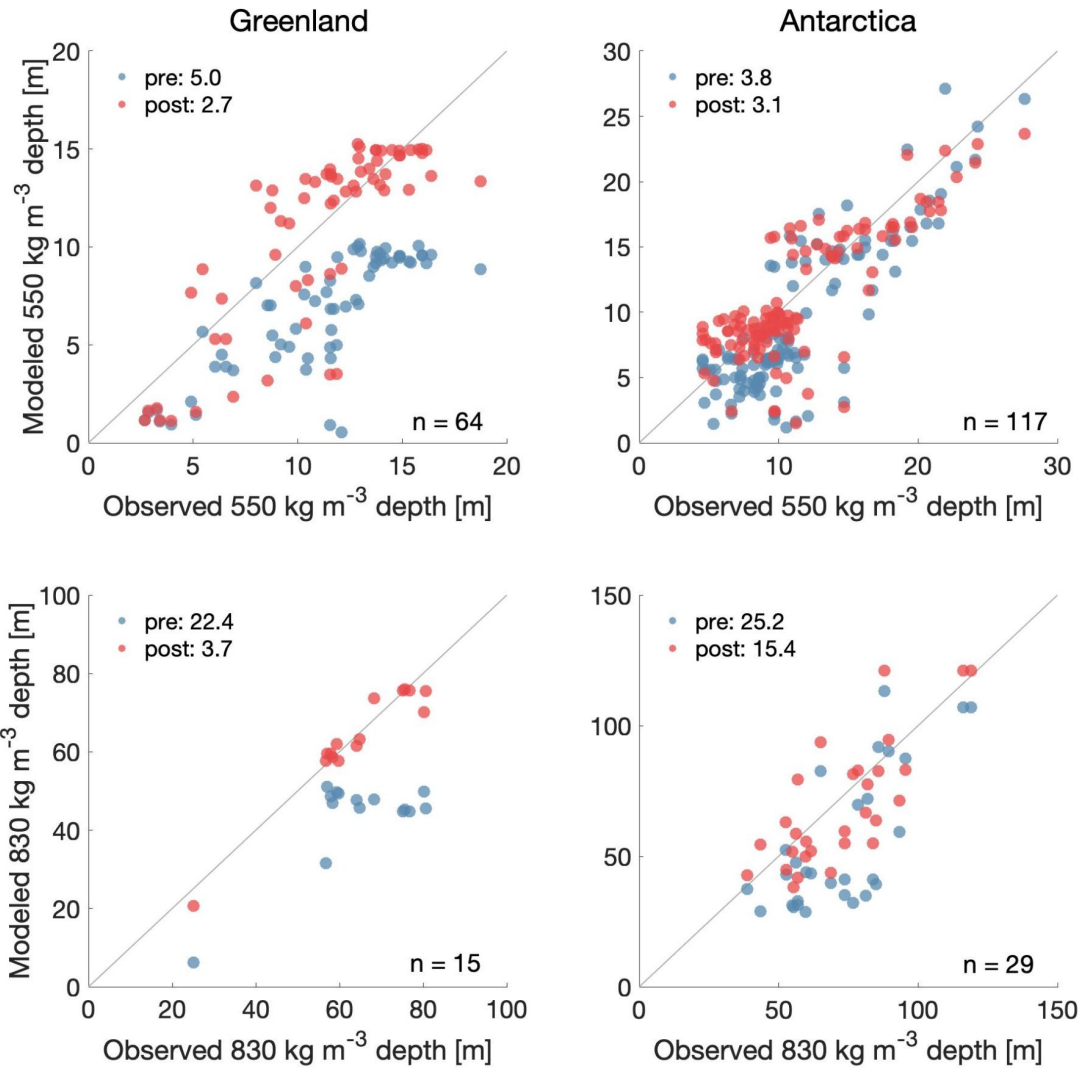
Figure 4: Comparison between modeled and observed 550 kg m⁻³ (top) and 830 kg m⁻³ (bottom) depths for the Greenland (left) and Antarctic (right) Ice Sheets for the locations of firn cores shown in Figure 3. Blue markers show pre-calibrated model agreement with observations, red markers show the post-calibrated model fit. The one-to-one line is shown by the black diagonal lines. Pre and post model calibration fits to observations (RMSE) are show in the top left of each panel.
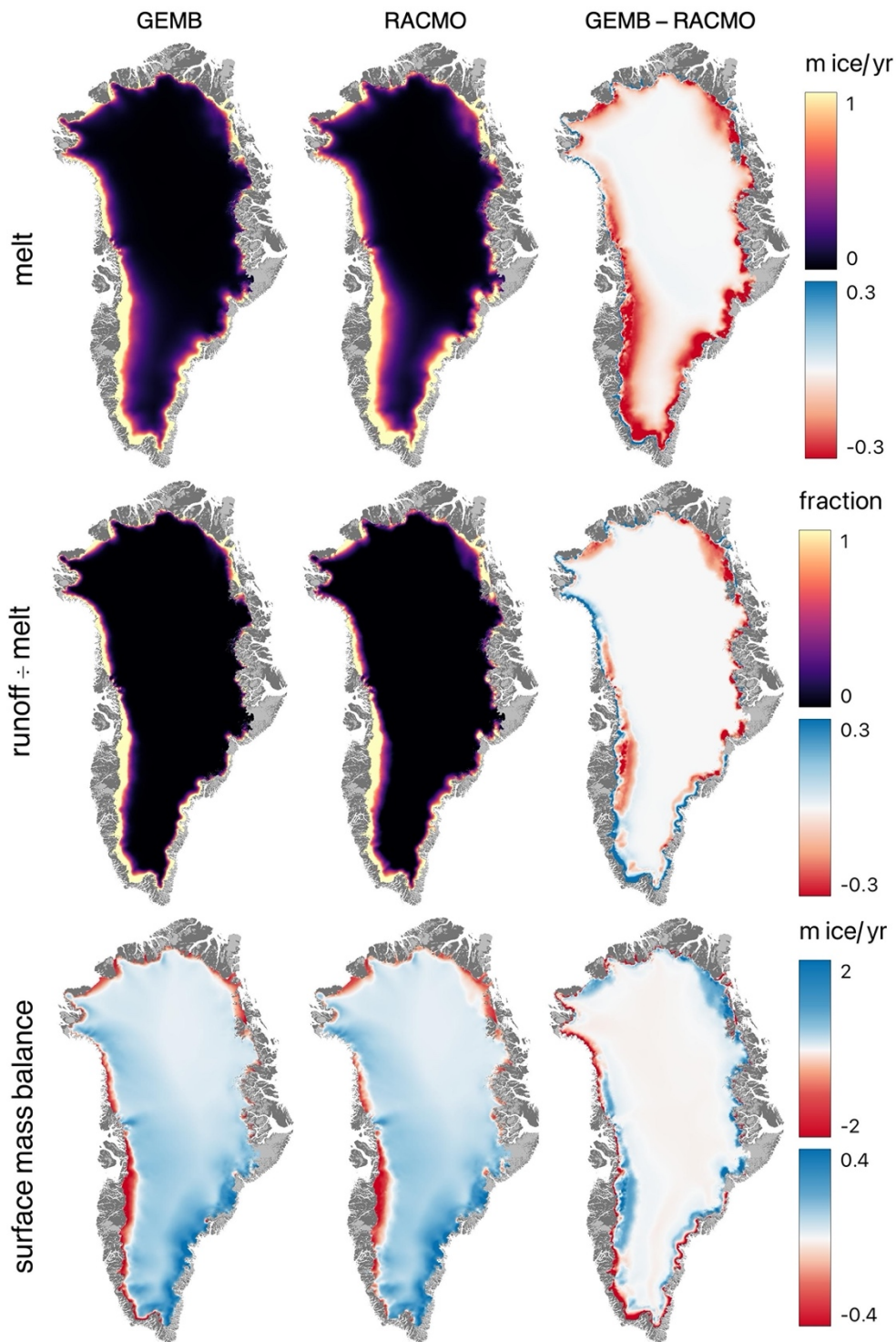
Figure 5: Mean 1979-2014 Greenland Ice Sheet GEMB (left) and RACMO (middle) model output in meters ice equivlent, and their difference (right).

035
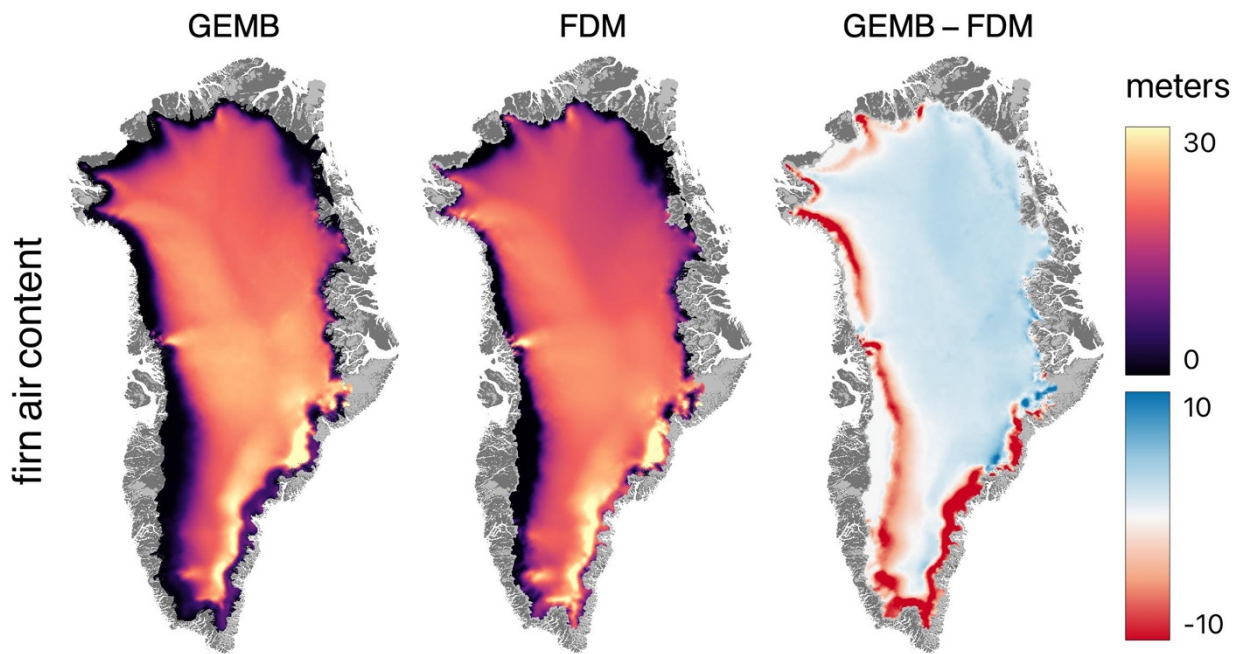
Figure 6: Mean 1979-2014 Greenland Ice Sheet GEMB (left) and IMAU-FDM (middle) firn air content, and their difference (right).

040
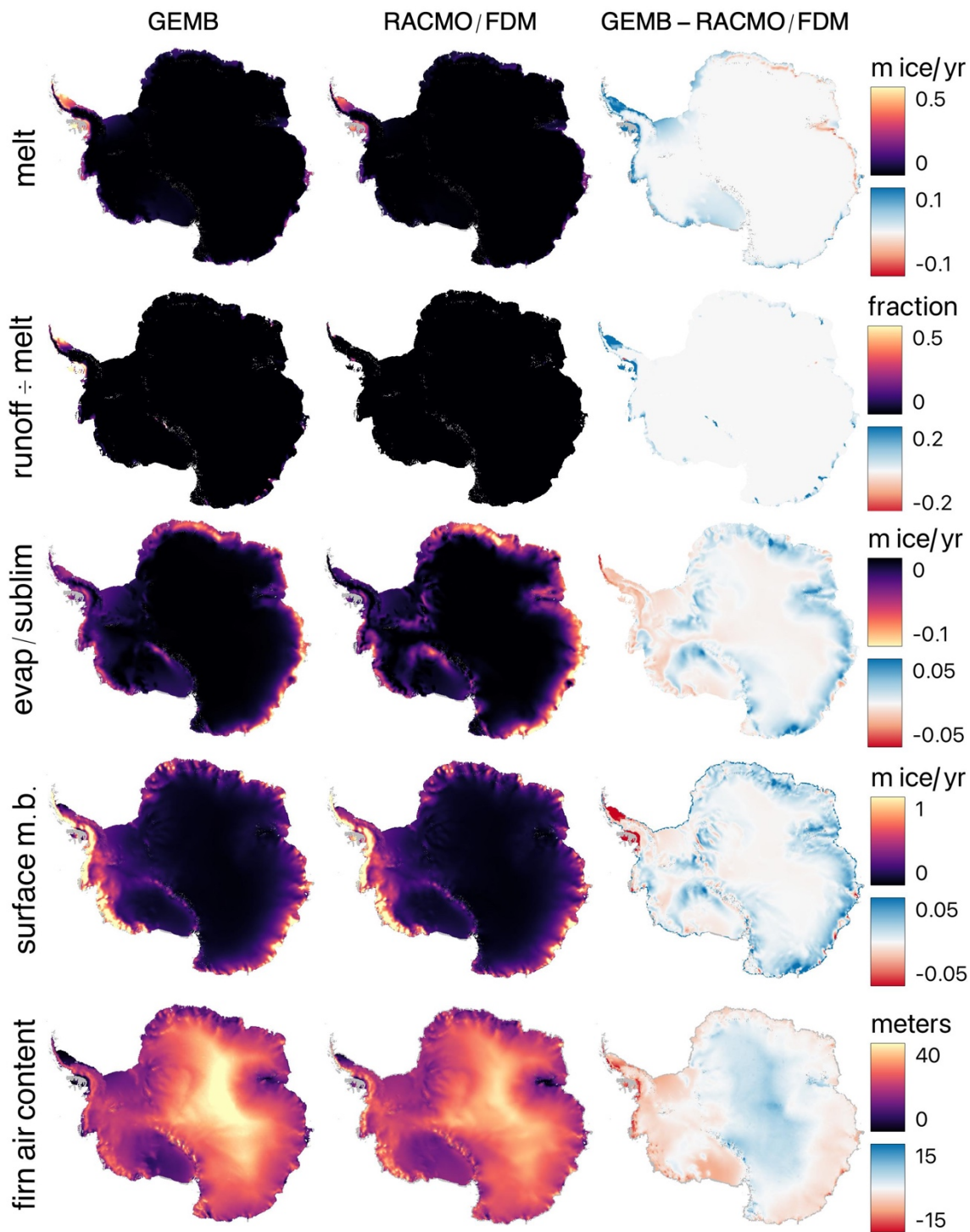
Figure 7: Mean 1979-2014 Antarctic Ice Sheet GEMB (left) and RACMO/IMAU-FDM (middle) model output in meters ice equivalent units, and their difference (right).
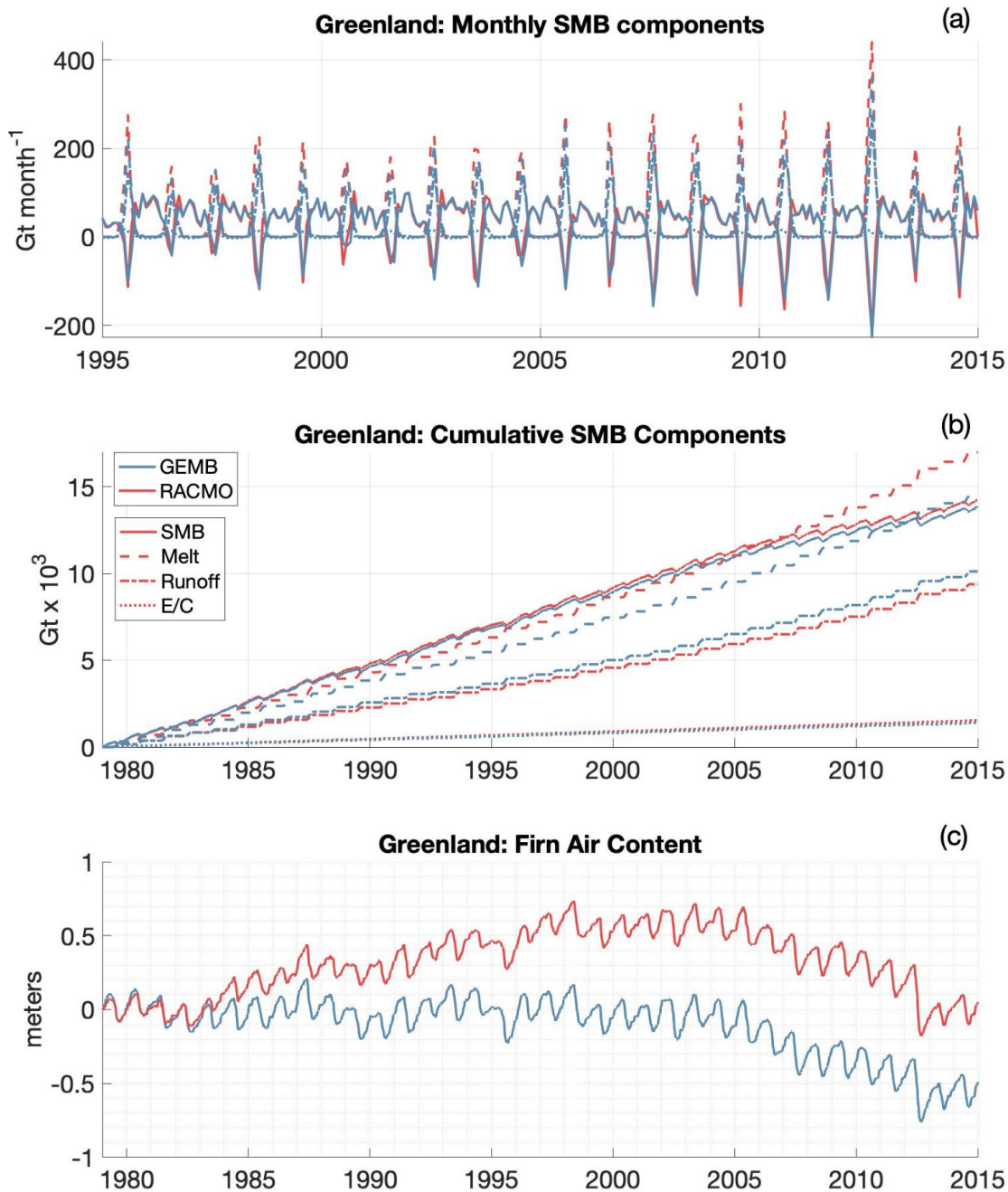
Figure 8: 1979-2014 Greenland Ice Sheet GEMB (blue) and RACMO (red) monthly (top) and cumulative (middle) model output. GEMB and IMAU-FDM average fin air content anomaly, relative to 1979, shown in bottom panel.
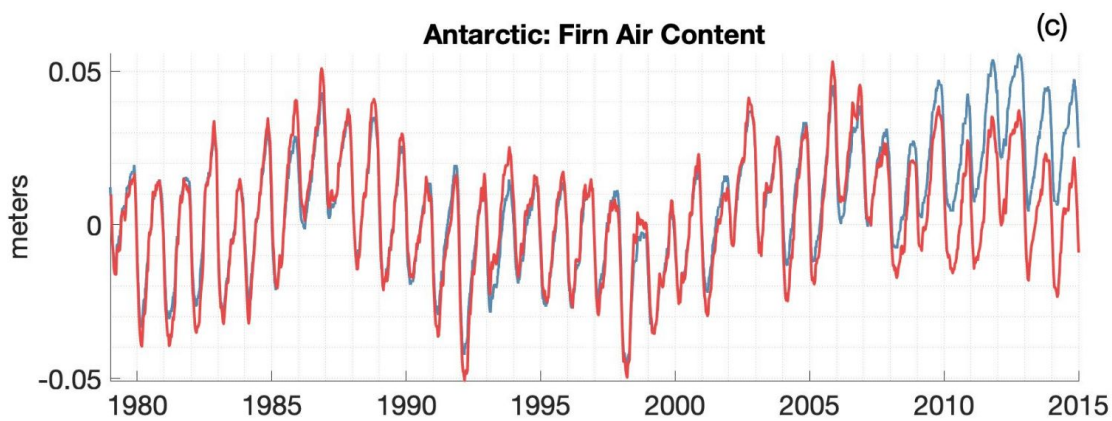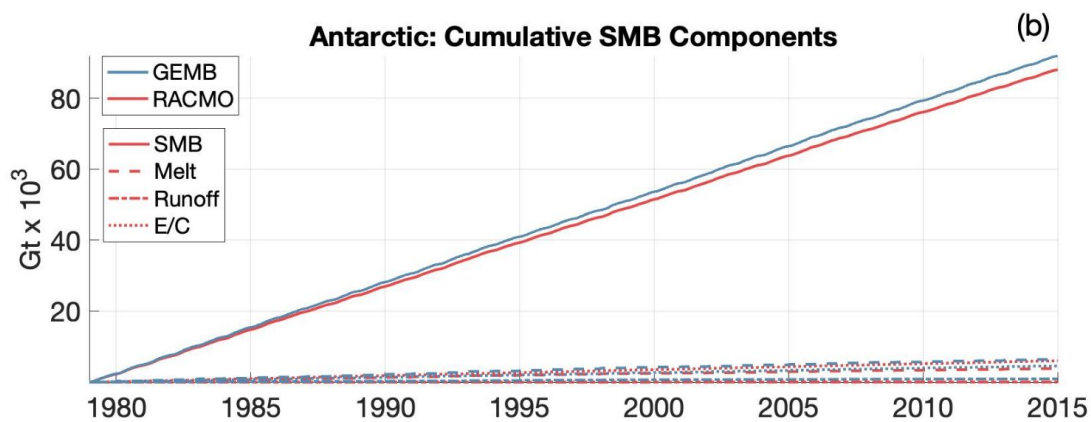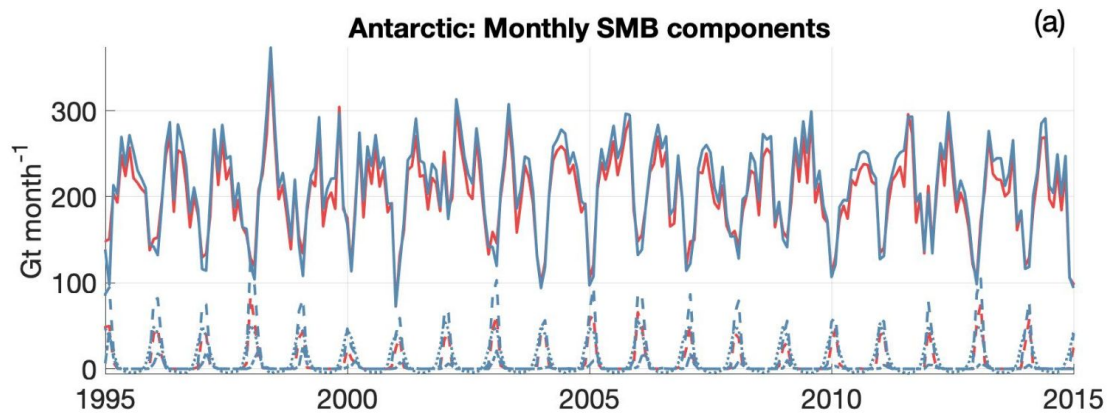
Figure 9: 1979-2014 Antarctic Ice Sheet GEMB (blue) and RACMO (red) monthly (top) and cumulative (middle) model output. GEMB and IMAU-FDM average fin air content anomaly, relative to 1979, shown in bottom panel.
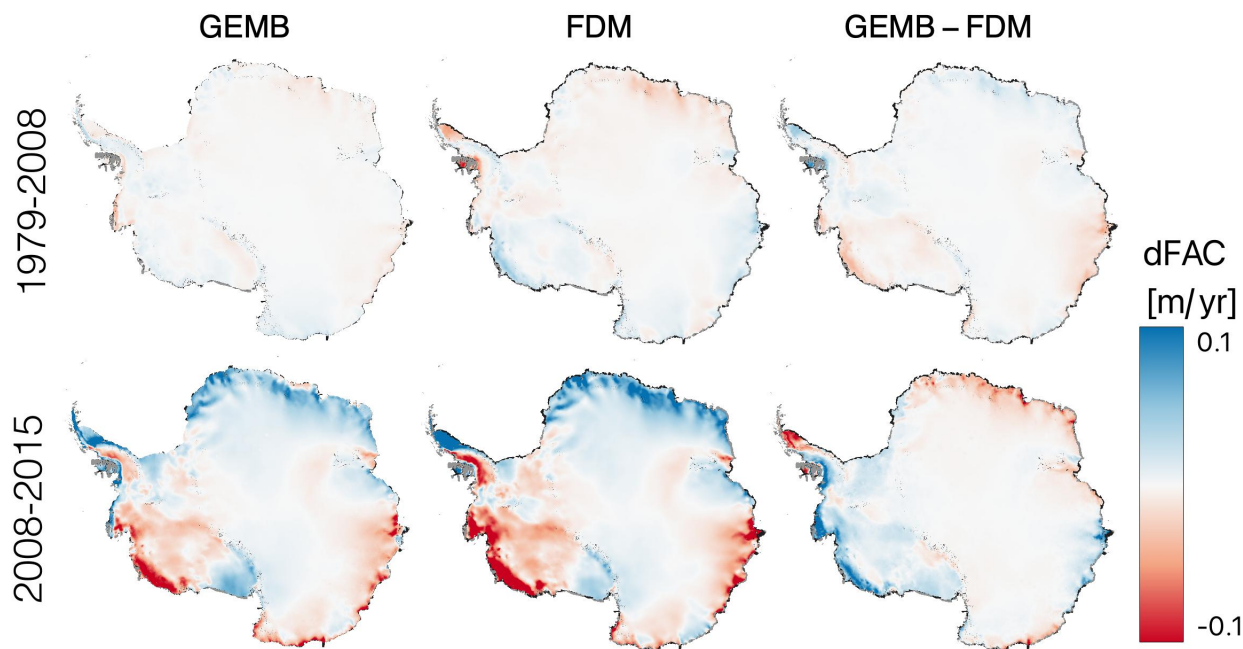
Figure 10: Rate of firn air content change (dFAC) for the Antarctic Ice Sheet as modeled by GEMB (left) and IMAU-FDM (center), and their difference (right). Rates for the period 1979-2008 are shown in the top panels and rates for the 2008-2015 period are shown in the bottom panels.
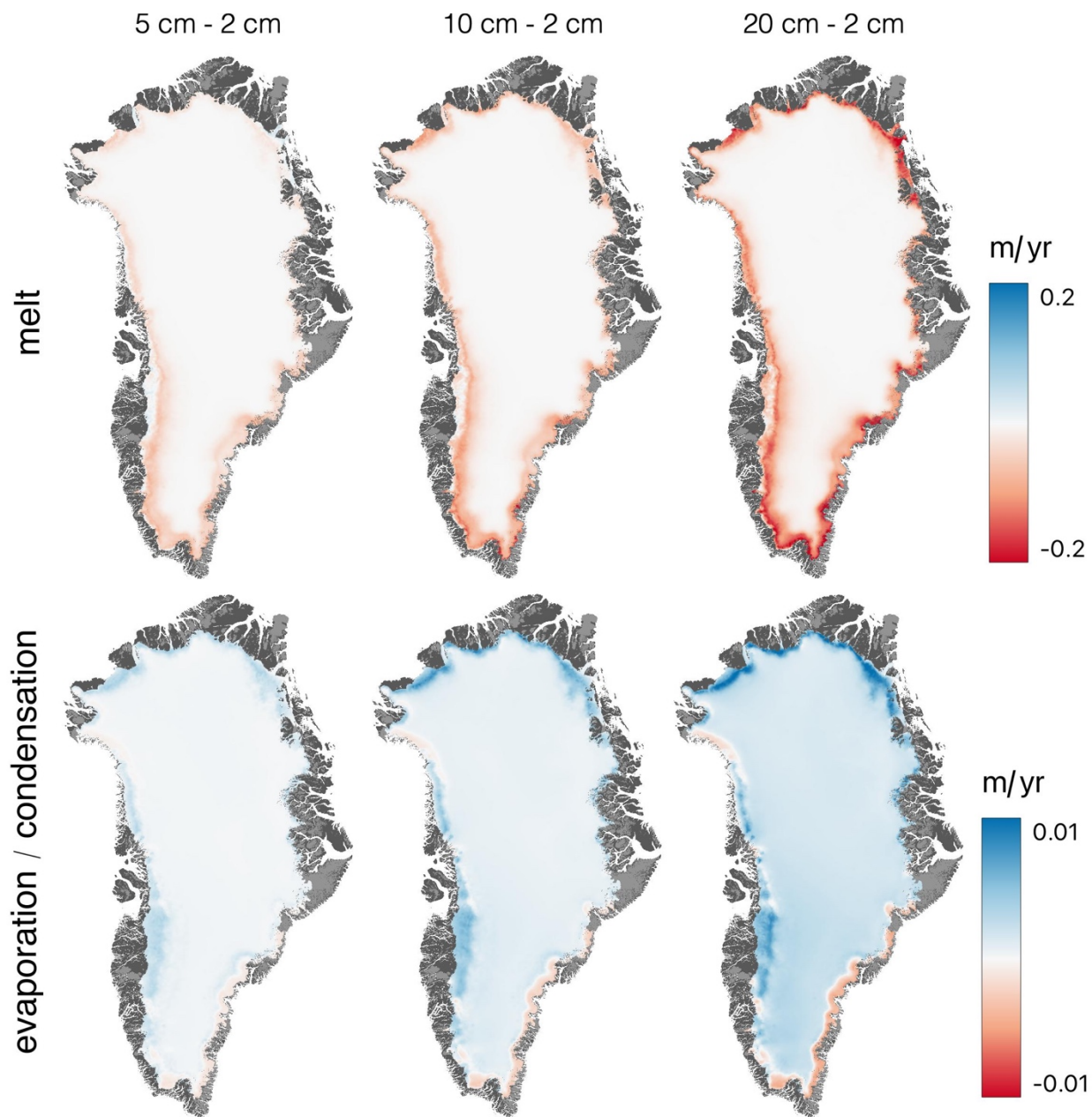
Figure 11: GEMB change in modeled rate of melt (top) and evaporation/condensation (bottom) for near-surface model layer depths (dz_{top}) of 5 cm, 10 cm, and 20 cm, relative to a near-surface model layer depth of 2 cm.
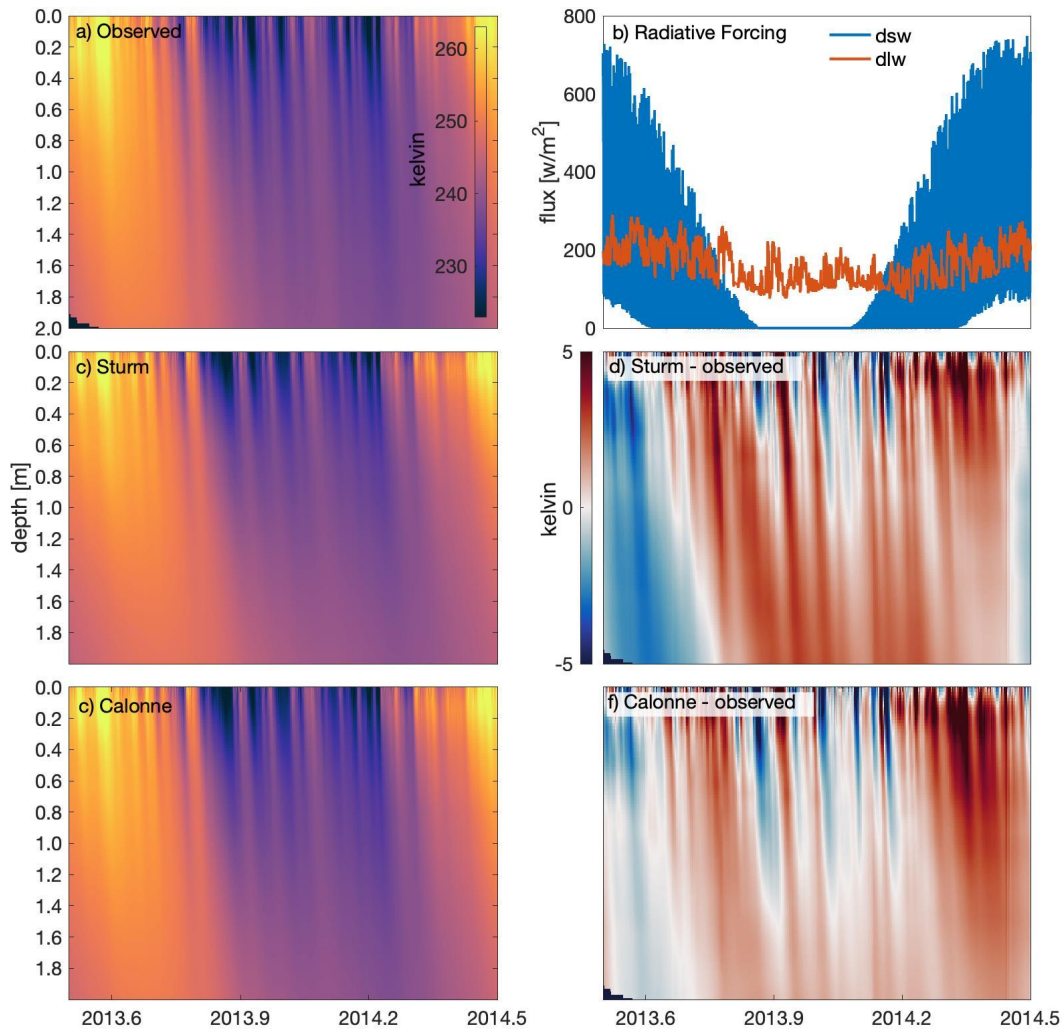
Figure 12: Observed and modeled daily near-surface (upper 2m) temperatures for Summit Station, Greenland (72.580° N and 38.459° W) from July 2013 to June 2014. Temperature profiles from (a) observations (Miller et al., 2017), (c) modeled using GEMB and Sturm et al. (1997) thermal conductivity and (e) modeled using GEMB and Calonne et al. (2011) thermal conductivity. (b) Observed downward shortwave (dsw) and longwave (dlw) radiation provided for context. Differences between temperature profiles for (d) GEMB-Sturm and observation and (f) GEMB-Calonne and observations. Note: All GEMB simulations are forced with RACMO model output (see Table 1) and therefore modeled temperature differences, relative to observations, are due to errors in forcing, model parametrizations and observations.
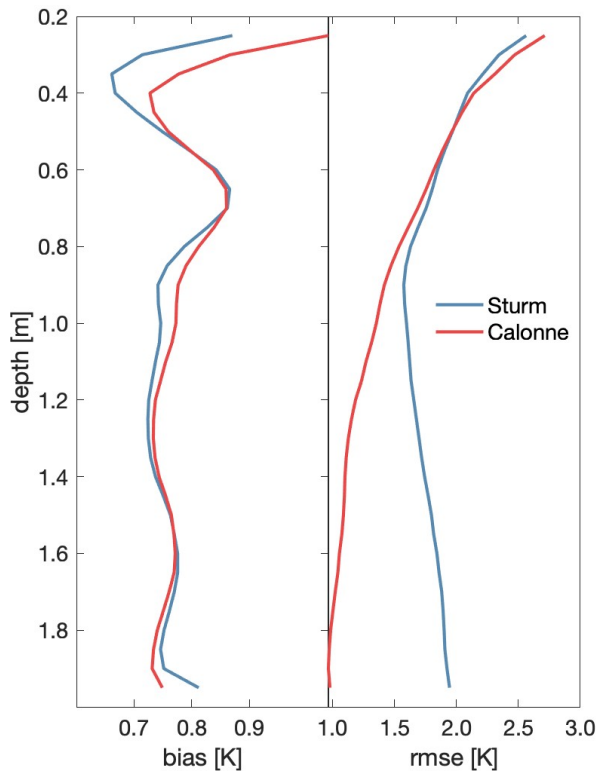
Figure 13: Mean bias (left) and rmse (right) in modeled near-surface temperatures as a function of depth, relative to observations (Miller et al., 2017). Daily GEMB model results using Sturm et al. (1997) and Calonne et al. (2011) thermal conductivity parameterizations for Summit Station, Greenland (72.580° N and 38.459° W) from July 2013 to June 2014.

075

Appendix A:

The following tables list the cores, taken from Montgomery et al. (2018) and Medley et al. (2022), and their citations. Those used for deep core calibration analysis (density of 830 kg m^{-3}) and shallow core calibration analysis (density of 550 kg m^{-3}) are marked in the corresponding 'Deep' and 'Shallow' columns. Cores without a 'Deep' or 'Shallow' designation were used for model evaluation.

Greenland

Latitude	Longitude	Deep	Shallow	Citation
77.45	-51.06		X	Baker, accessed 2015
66.181	-39.043	X	X	Koenig et al., 2014
65.775	-41.867		X	Miège et al., 2013
65.967	-41.481		X	Miège et al., 2013
66	-42.783		X	Miège et al., 2013
63	-48		X	Mosley-Thompson et al., 2001
63.149	-44.817		X	Mosley-Thompson et al., 2001
63.8	-45		X	Mosley-Thompson et al., 2001
66	-44.501		X	Mosley-Thompson et al., 2001
66.5	-42.5		X	Mosley-Thompson et al., 2001
67.5	-45		X	Mosley-Thompson et al., 2001
68	-41		X	Mosley-Thompson et al., 2001
69	-45		X	Mosley-Thompson et al., 2001
69	-38		X	Mosley-Thompson et al., 2001
69.2	-43		X	Mosley-Thompson et al., 2001
69.5	-34.5		X	Mosley-Thompson et al., 2001
71.05	-47.23		X	Mosley-Thompson et al., 2001
71.5	-45		X	Mosley-Thompson et al., 2001
71.926	-47.487		X	Mosley-Thompson et al., 2001
72.2	-49.4		X	Mosley-Thompson et al., 2001
73	-45		X	Mosley-Thompson et al., 2001
75	-51		X	Mosley-Thompson et al., 2001
75	-30		X	Mosley-Thompson et al., 2001
76	-53		X	Mosley-Thompson et al., 2001
65.1	-44.87	X	X	Mayewski and Whitlow, 2009

76.544	-66.204		X	Benson, 2013
77.3	-49.94		X	Benson, 2013
76.367	-67.992		X	Benson, 2013
76.402	-67.308		X	Benson, 2013
76.518	-66.387		X	Benson, 2013
76.722	-65.39		X	Benson, 2013
77.238	-62.328		X	Benson, 2013
77.217	-61.022		X	Benson, 2013
77.183	-60.393		X	Benson, 2013
77.128	-58.445		X	Benson, 2013
77.093	-57.818		X	Benson, 2013
70.105	-45.733		X	Benson, 2017
70.04	-46.133		X	Benson, 2017
69.917	-46.933		X	Benson, 2017
73.94	-37.63	X	X	Wilhelms, 2000a
75.25	-37.625	X	X	Wilhelms, 2000b
76.617	-36.403	X	X	Wilhelms, 2000c
80	-41.137	X	X	Wilhelms, 2000d
77.253	-49.217	X	X	Miller and Schwager, 2000a
76.004	-43.492	X	X	Miller and Schwager, 2000b
77.981	-37.704		X	Bolzan and Strobel, 1999a
72.212	-35.667		X	Bolzan and Strobel, 2001
71.602	-38.141		X	Bolzan and Strobel, 1999b
72.641	-35.944		X	Bolzan and Strobel, 1999c
72.349	-40.214		X	Bolzan and Strobel, 1999d
72.886	-39.157		X	Bolzan and Strobel, 1999e
71.927	-39.835		X	Bolzan and Strobel, 1999f
77.371	-55.927		X	Medley et al., 2022
72.567	-37.617	X	X	Medley et al., 2022
65.183	-43.833		X	Medley et al., 2022
77.95	-39.183	X	X	Medley et al., 2022
70.75	-35.958	X	X	Medley et al., 2022
70.635	-35.82	X	X	Medley et al., 2022
70.659	-35.479	X	X	Medley et al., 2022
70.677	-35.787		X	Medley et al., 2022

70.64	-35.618	X	X	Medley et al., 2022
71.759	-35.851	X	X	Medley et al., 2022
71.492	-35.881		X	Medley et al., 2022
71.155	-35.838		X	Medley et al., 2022
77.183	-61.167			Medley et al., 2022
71.75	-40.75			Medley et al., 2022
70.865	-35.838			Medley et al., 2022
76.983	-56.067			Medley et al., 2022

Antarctica

090

Latitude	Longitude	Deep	Shallow	Citation
-78.837	-116.31	X	X	Koenig and Brucker, 2011
-78.728	-114.73	X	X	Koenig and Brucker, 2011
-78.424	-115.29	X	X	Koenig and Brucker, 2011
-78.311	-113.79		X	Koenig and Brucker, 2011
-79.483	-112.09		X	Kreutz et al., 2011
-89.933	144.39		X	US ITASE, Mayewski and Dixon, 2013
-88.509	178.53		X	US ITASE, Mayewski and Dixon, 2013
-88.002	-107.98		X	US ITASE, Mayewski and Dixon, 2013
-86.84	95.31		X	US ITASE, Mayewski and Dixon, 2013
-86.503	-107.99		X	US ITASE, Mayewski and Dixon, 2013
-85.001	-105		X	US ITASE, Mayewski and Dixon, 2013
-82.08	101.96	X	X	US ITASE, Mayewski and Dixon, 2013
-82.001	-110.01		X	US ITASE, Mayewski and Dixon, 2013
-81.65	122.6	X	X	US ITASE, Mayewski and Dixon, 2013
-81.2	-126.17		X	US ITASE, Mayewski and Dixon, 2013
-80.62	-122.63	X	X	US ITASE, Mayewski and Dixon, 2013
-80.39	138.92	X	X	US ITASE, Mayewski and Dixon, 2013

-79.383	-111.24		X	US ITASE, Mayewski and Dixon, 2013
-79.16	-104.97		X	US ITASE, Mayewski and Dixon, 2013
-79.133	-122.27	X	X	US ITASE, Mayewski and Dixon, 2013
-79.036	149.68		X	US ITASE, Mayewski and Dixon, 2013
-78.733	-111.5		X	US ITASE, Mayewski and Dixon, 2013
-78.433	-115.92	X	X	US ITASE, Mayewski and Dixon, 2013
-78.12	-95.646		X	US ITASE, Mayewski and Dixon, 2013
-78.083	-120.08	X	X	US ITASE, Mayewski and Dixon, 2013
-77.88	158.46		X	US ITASE, Mayewski and Dixon, 2013
-77.88	158.66		X	US ITASE, Mayewski and Dixon, 2013
-77.844	-102.91	X	X	US ITASE, Mayewski and Dixon, 2013
-77.762	153.38		X	US ITASE, Mayewski and Dixon, 2013
-77.683	-124		X	US ITASE, Mayewski and Dixon, 2013
-77.612	-92.248		X	US ITASE, Mayewski and Dixon, 2013
-77.059	-89.138	X	X	US ITASE, Mayewski and Dixon, 2013
-76.097	-89.018	X	X	US ITASE, Mayewski and Dixon, 2013
-77.957	-95.962		X	Medley, B et al. (2013)
-76.952	-121.22		X	Medley, B et al. (2013)
-76.77	-101.74		X	Medley, B et al. (2013)
-79.354	-160.32		X	Conway (2003)
-79.486	-161.06		X	Conway (2003
-79.572	-161.57		X	Conway (2003
-74.12	1.6005		X	Medley et al., 2022
-82.811	18.9		X	Medley et al., 2022
-78.646	35.641		X	Medley et al., 2022
-82.066	54.89		X	Medley et al., 2022

-74.499	1.9612		X	Medley et al., 2022
-74.399	7.2175		X	Medley et al., 2022
-75.003	0.022667		X	Medley et al., 2022
-74.997	0.036167		X	Medley et al., 2022
-75.582	-3.4303		X	Medley et al., 2022
-75.933	7.213		X	Medley et al., 2022
-75.217	11.35		X	Medley et al., 2022
-74.855	-8.497		X	Medley et al., 2022
-75.001	-6.4983		X	Medley et al., 2022
-75	-4.4963		X	Medley et al., 2022
-74.949	-1.4945		X	Medley et al., 2022
-75.25	-6		X	Medley et al., 2022
-74.751	0.99983	X	X	Medley et al., 2022
-74.667	4.0017		X	Medley et al., 2022
-75.251	6.5017	X	X	Medley et al., 2022
-75.006	0.081867	X	X	Medley et al., 2022
-74.839	0.00995		X	Medley et al., 2022
-75.056	0.70402		X	Medley et al., 2022
-74.205	-9.7417	X	X	Medley et al., 2022
-79.615	-45.724		X	Medley et al., 2022
-71.457	-9.8607	X	X	Medley et al., 2022
-78.034	-58.691		X	Medley et al., 2022
-80	-55.5		X	Medley et al., 2022
-80.833	-56.588		X	Medley et al., 2022
-81.218	-57.203		X	Medley et al., 2022
-81.605	-57.888		X	Medley et al., 2022
-82.335	-57.827		X	Medley et al., 2022
-82.75	-58.692		X	Medley et al., 2022
-83.017	-59.575	X	X	Medley et al., 2022
-83.385	-60.063	X	X	Medley et al., 2022
-83.978	-60.36		X	Medley et al., 2022
-84.818	-59.635	X	X	Medley et al., 2022
-70.707	-8.4267		X	Medley et al., 2022
-70.617	-8.3667		X	Medley et al., 2022
-70.656	-8.2536		X	Medley et al., 2022

-70.246	26.335		X	Medley et al., 2022
-66.722	113.2		X	Medley et al., 2022
-74.5	123.17		X	Medley et al., 2022
-66.77	112.81		X	Medley et al., 2022
-72.654	-16.646		X	Medley et al., 2022
-73.594	-12.427		X	Medley et al., 2022
-73.816	-12.21	X	X	Medley et al., 2022
-74.014	-12.016		X	Medley et al., 2022
-74.017	-12.017		X	Medley et al., 2022
-74.351	-11.723		X	Medley et al., 2022
-74.767	-10.783		X	Medley et al., 2022
-75.1	-9.5		X	Medley et al., 2022
-76.533	6.1333		X	Medley et al., 2022
-70.698	44.332		X	Medley et al., 2022
-79.495	-120.03		X	Medley et al., 2022
-79.003	-119.57		X	Medley et al., 2022
-78.505	-119.72		X	Medley et al., 2022
-77.997	-120.02		X	Medley et al., 2022
-77.225	-119.85		X	Medley et al., 2022
-76.85	-118.23		X	Medley et al., 2022
-76.627	-117.62		X	Medley et al., 2022
-76.062	-116.95		X	Medley et al., 2022
-75.588	-116.45		X	Medley et al., 2022
-75.417	-116.3		X	Medley et al., 2022
-74.993	-116.12		X	Medley et al., 2022
-75.787	-118.75		X	Medley et al., 2022
-75.987	-121.08		X	Medley et al., 2022
-76.017	-123.68		X	Medley et al., 2022
-75.712	-125.63	X	X	Medley et al., 2022
-75.797	-128.07	X	X	Medley et al., 2022
-76.038	-130.17	X	X	Medley et al., 2022
-76.338	-132.3	X	X	Medley et al., 2022
-76.638	-134.5	X	X	Medley et al., 2022
-76.9	-136.87	X	X	Medley et al., 2022
-77.15	-139.3		X	Medley et al., 2022

-77.838	-139.95		X	Medley et al., 2022
-73.113	39.758		X	Medley et al., 2022
-71.194	45.979	X	X	Medley et al., 2022
-69.079	40.782		X	Medley et al., 2022
-75.084	2.501			Medley et al., 2022
-75.753	3.2828			Medley et al., 2022
-75.167	5.0033			Medley et al., 2022
-75.084	6.5			Medley et al., 2022
-74.449	-9.1807			Medley et al., 2022
-75.002	0.0678			Medley et al., 2022
-75.002	0.007			Medley et al., 2022
-75.001	8.0053			Medley et al., 2022
-79.483	-112.01			Medley et al., 2022
-80	-120			Medley et al., 2022
-72.762	-14.59			Medley et al., 2022
-73.457	-12.557			Medley et al., 2022
-75	2			Medley et al., 2022
-74.267	0.61667			Medley et al., 2022
-77.497	-120.02			Medley et al., 2022
-77.358	-141.77			Medley et al., 2022
-78.312	-138.17			Medley et al., 2022
-69.032	40.456			Medley et al., 2022
-82.892	-136.66			Medley et al., 2022
-75	147			Medley et al., 2022
-74	143			Medley et al., 2022
-73	142			Medley et al., 2022
-72	140			Medley et al., 2022
-71	139			Medley et al., 2022

References:

095   Baker I (2016) NEEM Firn Core 2009S2 Density and Permeability. (doi:10.18739/A2Q88G)

Benson C (2013) Greenland Snow Pit and Core Stratigraphy (Analog and Digital Formats) Boulder, Colorado USA: National Snow and Ice Data Center. https://doi.org/10.7265/N5RN35SK

100   Benson C (2017) Greenland Snow it and Core Stratigraphy. Carl S. Benson Collection. Coll. 2010011.
      Roger G. Barry Archives and Resource Center. National Snow Data Center. [Accessed June 2017].

      Bolzan, J F and Strobel, M (1999a): Oxygen isotope data from snowpit at GISP2 Site 15.
         doi:10.1594/PANGAEA.55511
105
      Bolzan, J F and Strobel, M (2001): Oxygen isotope data from snowpit at GISP2 Site 571.
         doi:10.1594/PANGAEA.59996

      Bolzan, J F and Strobel, M (1999b): Oxygen isotope data from snowpit at GISP2 Site 73.
110   doi:10.1594/PANGAEA.55516

      Bolzan, J F and Strobel, M (1999c): Oxygen isotope data from snowpit at GISP2 Site 37.
         doi:10.1594/PANGAEA.55513

115   Bolzan, J F and Strobel, M (1999d): Oxygen isotope data from snowpit at GISP2 Site 31.
         doi:10.1594/PANGAEA.55512

      Bolzan, J F and Strobel, M (1999e): Oxygen isotope data from snowpit at GISP2 Site 13.
         doi:10.1594/PANGAEA.55510
120
      Bolzan, J F and Strobel, M (1999f): Oxygen isotope data from snowpit at GISP2 Site 51.
         doi:10.1594/PANGAEA.55514

      Conway H (2003) Roosevelt Island Ice Core Density and Beta Count Data. (doi:10.7265/N55718ZW).
125
      Koenig L and Brucker L (2011) Satellite-Era Accumulation Traverse 2011 (SEAT11) snowpit density data.

      Koenig LS, Miège C, Forster RR and Brucker L (2014) Initial in situ measurements of perennial
      meltwater storage in the Greenland firn aquifer: Measurements of Greenland Aquifer. Geophysical
130   Research Letters 41(1), 81–85 (doi:10.1002/2013GL058083)

      Kreutz K (2011) Microparticle, Conductivity, and Density Measurements from the WAIS Divide Deep
      Ice Core, Antarctica. (doi:10.7265/N5K07264)

135   Mayewski P and Whitlow S (2009) Snow Pit and Ice Core Data from Southern Greenland, 1984, Version
      1.0. (doi:10.5065/D6S180MH)

140 Medley B, Joughin I, Das SB, Steig EJ, Conway H, Gogineni S, Criscitiello AS, McConnell JR, Smith BE, van den Broeke MR, Lenaerts JTM, Bromwich DH and Nicolas JP (2013) Airborne-radar and ice-core observations of annual snow accumulation over Thwaites Glacier, West Antarctica confirm the spatiotemporal variability of global and regional atmospheric models. Geophys. Res. Lett. 40(14), 3649–3654 (doi:10.1002/grl.50706)

145 Medley, B., Neumann, T. A., Zwally, H. J., Smith, B. E., & Stevens, C. M. (2022). Simulations of firn processes over the Greenland and Antarctic ice sheets: 1980–2021. The Cryosphere, 16(10), 3971–4011. https://doi.org/10.5194/tc-16-3971-2022. Personal Communication.

Miège C, Forster RR, Box JE, Burgess EW, McConnell JR, Pasteris DR and Spikes VB (2013) Southeast
150 Greenland high accumulation rates derived from firn cores and ground-penetrating radar. Annals of Glaciology 54(63), 322–332 (doi:10.3189/2013AoG63A358)

Miller, H. and Schwager, M. (2000a): Density of ice core ngt37C95.2 from the North Greenland Traverse. doi:10.1594/PANGAEA.57798
155
Miller, H. and Schwager, M. (2000b): Density of ice core ngt42C95.2 from the North Greenland Traverse. doi:10.1594/PANGAEA.57655

Montgomery, L., L. Koenig, and P. Alexander (2018): The SUMup dataset: Compiled measurements of
160 surface mass balance components over ice sheets and sea ice with analysis over Greenland. Earth Syst. Sci. Data, 10, 1959-1985, doi:10.5194/essd-10-1959-2018.

Mosley-Thompson E, McConnell JR, Bales RC, Li Z, Lin P-N, Steffen K, Thompson LG, Edwards R and Bathke D (2001) Local to regional-scale variability of annual net accumulation on the Greenland ice
165 sheet from PARCA cores. J. Geophys. Res. 106(D24), 33839–33851 (doi:10.1029/2001JD900067)

US International Trans-Antarctic Scientific Expedition (US ITASE) Glaciochemical Data, Version 2-Mayewski, P. A. and D. A. Dixon (2013), US International Trans-Antarctic Scientific Expedition (US ITASE) Glaciochemical Data. Version 2. [US_ITASE_Core Info-SWE-Density_2013.xlsx]. Boulder,
170 Colorado USA: National Snow and Ice Data Center.

Wilhelms, Frank (2000a): Density of ice core ngt03C93.2 from the North Greenland Traverse. doi:10.1594/PANGAEA.56560

175 Wilhelms, Frank (2000b): Density of ice core ngt06C93.2 from the North Greenland Traverse. doi:10.1594/PANGAEA.57153

Wilhelms, Frank (2000c): Density of ice core ngt14C93.2 from the North Greenland Traverse. doi:10.1594/PANGAEA.56615

180

Wilhelms, Frank (2000d): Density of ice core ngt27C94.2 from the North Greenland Traverse. doi:10.1594/PANGAEA.57296